Experimental and numerical investigation of sandstone deformation under cycling loading relevant for underground energy storage

Naderloo, Milad; Ramesh Kumar, Kishan; Hernandez, Edgar; Hajibeygi, Hadi; Barnhoorn, Auke

DOI
10.1016/j.est.2023.107198

Publication date
2023

Document Version
Final published version

Published in
Journal of Energy Storage

Journal of Energy Storage 64 (2023) 107198

Contents lists available at ScienceDirect

Journal of Energy Storage

journal homepage: www.elsevier.com/locate/est

Research papers

Experimental and numerical investigation of sandstone deformation under cycling loading relevant for underground energy storage

Milad Naderloo [*,1], Kishan Ramesh Kumar[1], Edgar Hernandez, Hadi Hajibeygi, Auke Barnhoorn

Faculty of Civil Engineering and Geosciences, Department of geoscience and engineering, Delft University of Technology, Stevinweg 1, 2628CV, Delft, The Netherlands

ARTICLE INFO

Keywords:
Subsurface energy storage
Geomechanics
Nonlinear material deformation
Acoustic emissions
Sandstone

ABSTRACT

Considering the storage capacity and already existing infrastructures, underground porous reservoirs are highly suitable to store green energy, for example, in the form of green gases such as hydrogen and compressed air. Depending on the energy demand and supply, the energy-rich fluids are injected and produced, which induces cyclic change of state-of-the-stress in the reservoir and its surrounding. Detailed analyses of the geo-mechanical deformations under variable storage conditions i.e., storage frequency and fluid fluctuating pressures, are crucially important for safe and efficient operations. The present work presents an integrated analysis, based on experimental and constitutive modeling aspects, to investigate sandstones' geomechanical response to cyclic loading relevant to underground energy storage (UES). To this end, sandstone rock samples were subjected to cyclic loading above and below the onset of dilatant cracking under different frequencies and loading amplitudes. Axial strains and Acoustic Emissions (AE) were measured in both regimes to quantify the total deformation (strain) of the rock and its AE characteristics. It is found that the inelastic strain and number of AE events is the highest in the first cycle and reduce subsequently cycle after cycle. Moreover, cyclic inelastic deformations are affected by the mean stress, amplitude, and frequency of the stress waveform. On the one hand, the higher the mean stress and the amplitude, the higher the total inelastic strains. On the other hand, the lower the frequency, the higher the total inelastic strain. From the modeling perspectives, five types of deformation mechanisms were identified based on the governing physics: elastic, viscoelastic, compaction-based cyclic inelastic, inelastic brittle creep, and dilatation-based inelastic deformation. To model elastic, viscoelastic, and brittle creep, the Nishihara model was used. A cyclic modified cam clay model (MCC) and hardening–softening model were applied to capture plastic deformation. The results show a very good fit of the constitutive model with the experimental results, which could help in studying the response of reservoirs to injection and production.

1. Introduction

In the advent of climate change, a successful transition towards cleaner renewable energy calls for effective large-scale (i.e., in the order of TWh) storage technologies [1]. To overcome the challenge of intermittency in renewable energy, subsurface storage technology needs to be efficiently developed [2]. One of the established options is underground gas storage (UGS), in which imported gas is stored in subsurface reservoirs during the summer when prices and demand are low, for heating during winter [3–5]. However, global concerns about climate change are driving more attention to renewable energy sources and storage, such as compressed air energy storage "CAES" [6], underground hydrogen storage "UHS" [7–9], and aquifer thermal energy storage (ATES) [10]. A detailed review of energy storage types can be found in Refs. [11–14]. The geological formations such as porous reservoirs and salt caverns, has proved to be a good option for storing energy-rich or energy-carrier fluids, such as compressed air, hot water, and hydrogen [15–18]. Porous media, such as depleted gas reservoirs, can provide significantly more storage capacity in different locations [19,20]. The high permeability and availability of porous rocks, such as sandstone reservoirs, make them promising for storage [17,21,22]. Therefore, further research on porous rocks, especially sandstone reservoirs, which contain a large-fraction of the world reserves, is crucial to designing and operating underground storage [23].

Subsurface storage technology is based on the injection and production of energy-rich fluids into underground reservoirs depending

* Corresponding author.
E-mail address: m.naderloo@tudelft.nl (M. Naderloo).
[1] Equal contribution.

https://doi.org/10.1016/j.est.2023.107198
Received 6 February 2023; Received in revised form 6 March 2023; Accepted 17 March 2023
Available online 23 March 2023

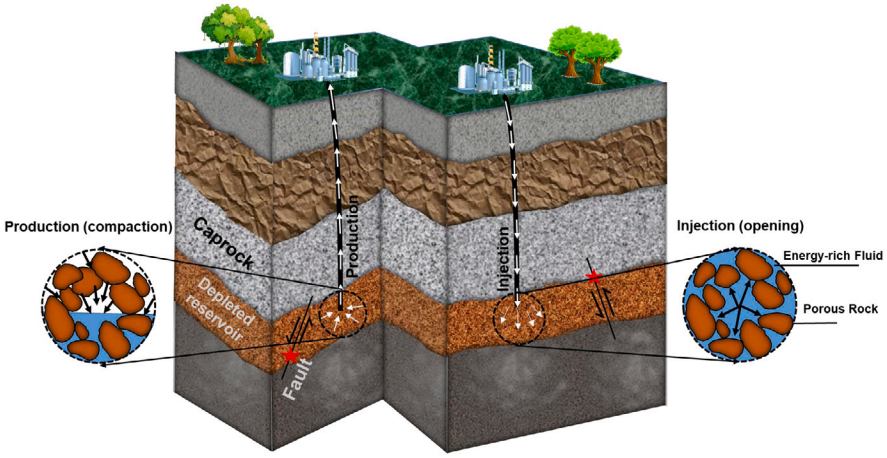

Fig. 1. Illustration of potential geological storage (depleted gas reservoir) sites for energy-rich fluids.

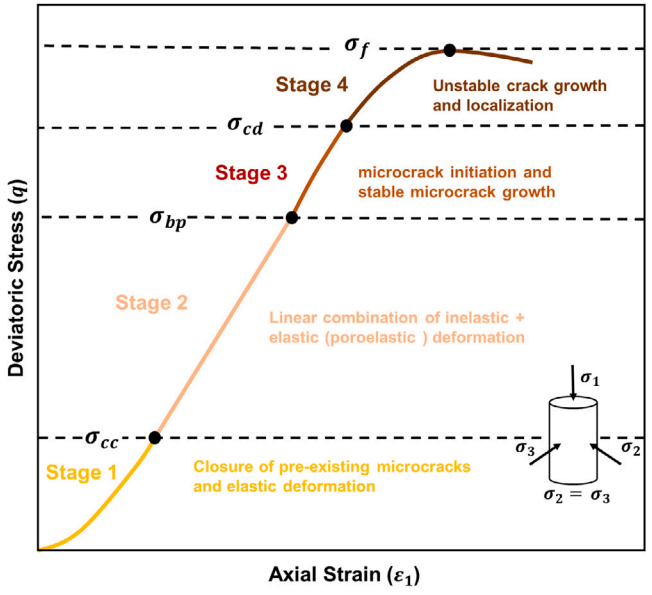

Fig. 2. Stress–strain curve showing deformation stages of Red Felser sandstone under the condition of constant confining pressure (10 MPa). The four stages of stress levels are: the initial crack closure (σ_{cc}), brittle yield point stress (σ_{bp}), crack damage stress (σ_{cd}) and maximum strength (σ_f). . (For interpretation of the references to color in this figure legend, the reader is referred to the web version of this article.)

on the demand and supply [21,24], resulting in cyclic loading as shown in Fig. 1. Thus, the reservoir experiences cyclic changes in porous pressure and temperature. As a result, the in-situ effective stresses are altered accordingly, which influences the stress conditions on the reservoir rock and surrounding elements, such as caprock, faults, and wells [25–29]. For instance, a decrease or increase in fluid pressure can induce fault reactivation and seismicity (earthquakes) by perturbing the stress path [30,31]. The pressure fluctuation during storage can also induce subsidence, which damages the infrastructures nearby [32,33]. Therefore, it is essential to understand about deformation behavior of sandstone reservoirs and the effect of all the different injection/depletion-related parameters, including amplitude and frequency of cycles, to reduce the risk of delaying projects and optimize the utility of the energy storage operations [20].

Many experimental researchers have identified the mechanical behavior and deformation process of sandstone subjecting to conventional deviatoric testing [34–38]. This behavior is normally represented in terms of mean effective stress versus total porosity reduction or deviatoric stress versus axial deformation [39,40]. As shown in Fig. 2, the four stages of the Red Felser sandstone deformation up to reaching maximum strength are as follows [41,42]:

- Stage 1 (from the start to σ_{cc}): A non-linear behavior that reflects the closure of pre-existing cracks or damage alongside poro-elastic deformation.
- Stage 2 (from σ_{cc} to σ_{bp}): Near-linear behavior of sandstone which is known as purely elastic (poroelastic) deformation.
- Stage 3 (from σ_{bp} to σ_{cd}): The deformation shows non-linear behavior due to the initiation of new microcracks and stable crack growth.
- Stage 4 (from σ_{cd} to σ_f): The concave-down behavior in this regime is attributed to the onset of grain crushing, unstable crack growth, and shear crack localization.

Among different stages of deformation, stage 2 and the early part of stage 3 are important from an energy storage perspective. This is because all the energy storage systems should be operated below the yield point and within a safe zone to avoid failure and accumulation of inelastic deformation. Recent and previous experimental studies on applying cyclic loading have reported a significant contribution of inelastic deformation within stage 2 (fully linear zone), where the inelastic deformation can contribute from 20% to 70% of total deformation [42–45]. Thus, applying cyclic stress conditions can change the deformation mechanism of sandstone resulting in an accumulation of inelastic deformation and damage as the number of cycles increases, which accordingly influences mechanical, acoustic and other petrophysical properties [46–48]. The intensity and quantity of this change (damage) can be different according to stress level (Fig. 2) and cyclic-related parameters (amplitude and frequency of cycles).

A few researchers have focused on the effect of frequency of the cycles on sandstone [49–52]. They observed that by increasing the frequencies, damage and axial deformation decrease because of the prevention of the growth of new fractures in both compaction and inelastic stages. Also, a few researchers studied the effect of the amplitude of cycles on the lifetime of sandstone [46,53,54]. Studies into the effect of amplitude indicated that by increasing the stress amplitude, the residual strain accumulation rate in sandstone is increased, resulting in reduced fatigue life. Also, some studies have focused on the evolution of the mechanical properties of reservoir sandstone under different operating conditions [49,55–57]. Nevertheless, there are very few studies into the effect of cyclic-related parameters on the quantification of inelastic deformation from the perspective of energy storage.

In addition to the study of mechanical evolution itself under cyclic loading, some studies have attempted to use non-destructive methods

such as active and passive acoustics to monitor and correlate the number of cycles and cycles pattern with different acoustic parameters [48,58–61]. The Acoustic Emission (AE) technique is a non-destructive method defined as a transient elastic wave that is produced by released strain energy due to an internal phenomenon such as grain slides or crushing, plastic deformation, and microcrack initiation [62,63]. However, the AE technique has not yet been used to investigate the different types of elastic and inelastic deformation occurring in sandstone under cyclic loading.

In this work, we perform cyclic triaxial experiments on the Red Felser sandstone to quantify the inelastic deformation occurring in sandstone under different cyclic-related parameters. Besides, the effect of the stress regime was investigated on types of deformation (time-dependent and instantaneous) and inelastic deformation. In particular, we focus on the evolution of the axial inelastic strain, the number of generated AE events per cycle, and the correlation between the cumulative inelastic strain and cumulative AE numbers. Experimental studies have limitations associated with the geometry scale, time scale, and heterogeneity. Thus, to explore the effects of cyclic loading for longer time scales and large-scale reservoir models, constitutive models are usually developed based on experimental data to determine the different types of deformations (elastic, viscoelastic, creep, plastic).

Several forms of constitutive models have been taken into account for various types of rocks in the literature, including rock salt [64,65] and generalized models for brittle rocks [66]. Models such as the Maxwell model, the Kelvin-Voigt model, and the Fractional Maxwell model, attempt to consider the viscoelastic strain in rocks [67,68]. The time-dependent plastic creep strain is modeled using a power law for rock-salt, brittle porous rocks [18,69,70] and also modeled using viscoplastic deformation where the plastic strain starts accumulating above a certain stress level [71–74]. Lastly, in a generalized form for soil and rocks, the time-independent plastic strain has been considered [42,70,75–80]. Recently Modified Cam Clay model (MCC) [76] was employed to explain the inelastic deformation of sandstone below the brittle yield point [42]. However, there are very few attempts by researchers trying to quantify all the deformations observed in different stress regimes under cyclic loading on sandstone.

To address the above challenge, based on the observed experimental results, different constitutive models were conglomerated in this work. The Kelvin-Voigt model has been employed to quantify viscoelastic deformation. Time-independent plastic deformation in the near-linear regime is accounted for using the MCC model, which is further modified, inspired by [76], to account for the effect of cyclic loading. A hardening–softening model is considered for time-independent plastic deformation in a brittle regime [75,78]. Thus, the appropriate plasticity and creep model is employed depending on the measured brittle yield point from the experiments.

The rest of the paper is structured as follows. First, the experimental setup and methodology are described. Next, the employed constitutive laws are presented in detail. Experimental results are further elaborated, showing the effect of amplitude, frequency of the cycles, and stress regime on axial deformation and acoustic emission characteristics. Then, numerical results are calibrated and compared with experimental data. Based on the experimental and numerical results, conclusions are drawn.

2. Experimental design and test scheme

2.1. Sample preparation and loading apparatus

Red Felser sandstone was selected as the reservoir rock for the cyclic experiments. Red Felser sandstone is part of the Rotliegend formation, which originates from near Kaiserslautern, Germany. Its lithology and geological age make it relevant for storage applications in the Slochteren sandstone in the Netherlands. All samples were drilled 30 mm in diameter from a unique rock slab to ensure the best possible reproducibility between samples. Next, the samples were cut to a nominal length of approximately 70 mm. The average density and porosity of the samples were 2.1 ± 0.015 g/cm^3 and 21.14 ± 0.7%. An example of prepared Red Felser sandstone is shown in Fig. 4a.

To carry out the triaxial cyclic test, also known as the deviatoric cyclic test, a servo-control loading machine manufactured by the TU Delft was used (Fig. 3) to apply axial stress (σ_1). In order to apply the confining pressure or horizontal stress ($\sigma_2 = \sigma_3$), an instrumented triaxial cell as the one shown in Fig. 3 was used together with the loading machine. The triaxial cell includes a special silicon jacket that, in addition to providing isolation between the confining fluid and the rock sample, has a total of 6 piezoelectric transducers. The vertical deformation of the rock sample is measured by two Linear Variable Displacement Transformer ”LVDT” (Fig. 3).

2.2. Acoustic emission monitoring

The Acoustic emission (AE) technique was used to detect the AE events and their correlation with inelastic deformation. The silicon jacket was instrumented with an array of 6 piezoceramic transducers to record AE events originating from rock samples during stress cycling. Next, the Richter system, a continuous data acquisition system was used to record AE activities captured by piezoelectric transducers. A schematic illustration of the AE system is given in Fig. 3. The AE system consists of 4 units that can be synchronized to provide a fully expandable system with up to 20 channels. The ExStream software controls the acoustic emission system, whereas the Insite Seismic Processor software processes and manages the raw waveform data. A trigger logic is used to convert continuous waveform data into single waveforms for further analysis. Concerning background noise, the number of sensors (6 sensors were used), and array distribution, if three or more transducers exceed a voltage threshold of about 0.05 V within a time window of 480 μs and a sampling rate of 2 MHz, it can be recorded as an event.

2.3. Testing protocol

In the beginning, two monotonic deviatoric tests were carried out at 10 MPa confining pressure until macroscopic sample failure occurred to determine the failure stages and deformation behavior of the Red Felser sandstone. After these tests, different deformation stages of the Red Felser sandstone were determined, such as stage 1, stage 2, and the start of stage 3, to design our experimental protocol (Fig. 4b).

In total, 12 deviatoric cyclic tests were carried out, and all the samples were fully saturated with water before the tests. Regarding the deviatoric cyclic test, two mean axial stresses ($\sigma_{1,mean}$) were selected: one right at the start of stage 2 equal to 38 MPa (Elastic regime) and the second one right above the brittle yield point equal to 85 MPa (brittle regime). According to the stress–strain and stress-time derivatives, the brittle yield point is estimated to be 84.2 MPa (Fig. 4b). For the frequencies, three scenarios were evaluated F1 = 0.014 Hz (1.2 min/cycle), F2 = 0.0014 Hz (12 min/cycle), and F1 = 0.0002 Hz (83 min/cycle). It is difficult to apply real-field relevant frequencies (seasonal timescales) in our laboratory. We aimed to have a set of frequencies that could help shedding new lights on the time-dependent deformations, and their consistent modeling concepts. It should be mentioned that frequency is adjusted by increasing or decreasing the loading rate. Finally, two axial stress amplitudes were tested A1 = 20 MPa and A2 = 5.9 MPa. The latter is equivalent to the yearly pore pressure changes in the NORG gas field [81]. These conditions were permuted, leading to 12 cyclic tests with a maximum of 8 cycles Table 1.

A triangular waveform was selected to approximate the cyclic stress behavior of underground storage field applications. Thus the maximum stress of the waveform corresponds to the minimum pore pressure (compaction), while the minimum stress refers to the maximum stored volume or pore pressure (opening). The main parameter that defines

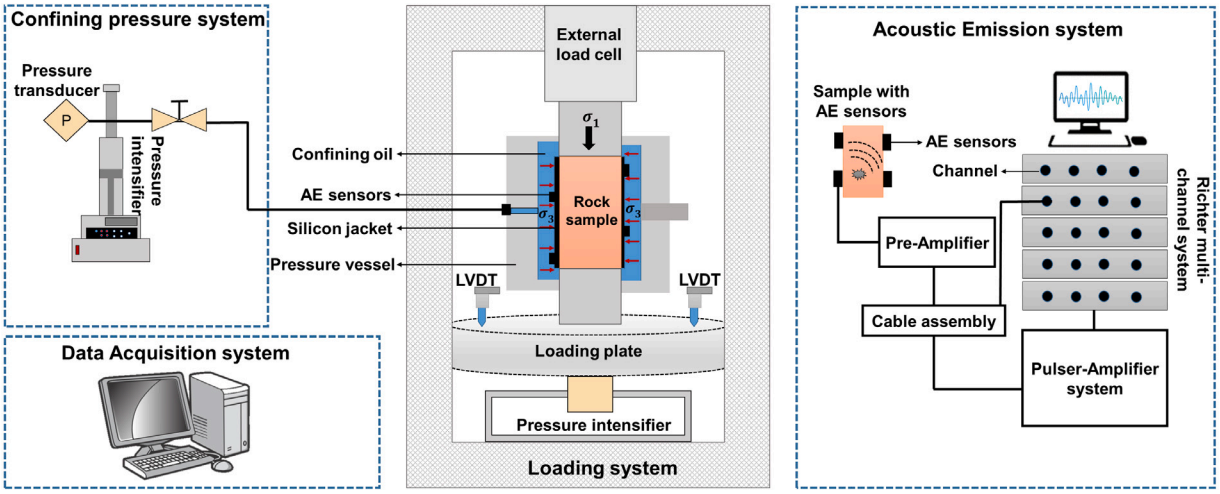

Fig. 3. Schematic illustration of the experimental setup including loading system, data acquisition, and AE system.

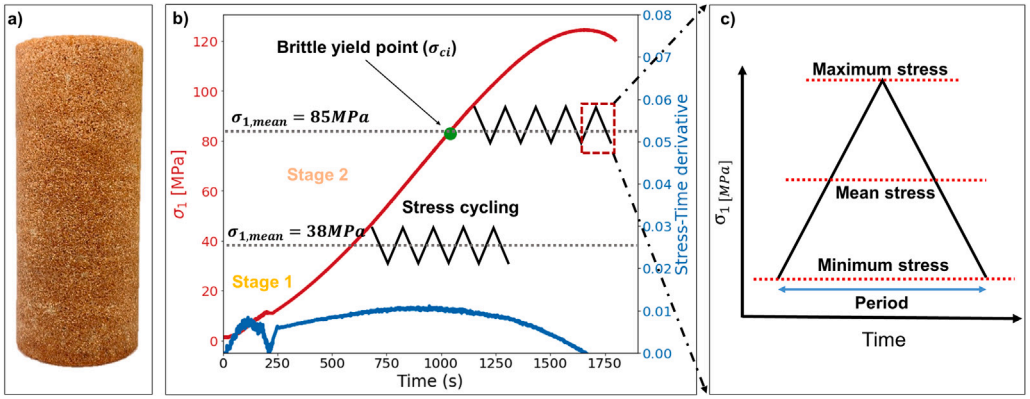

Fig. 4. Illustration of the experimental protocol and Red Felser sandstone; (a) the Red Fleser sandstone sample after preparation, (b) The stress-time curve together with mean stress levels (cycling stress level), and (b) The triangular waveform of stress. (For interpretation of the references to color in this figure legend, the reader is referred to the web version of this article.)

Table 1
Information about rock samples, cyclic parameters, total inelastic strain ($\epsilon_{1,total}^{inelastic}$), the total number of AE (N_{AE}), and average events amplitude ($A_{AE}^{average}$) for the cyclic tests and multi-stage (MS) creep test with confining pressure of σ_3 = 10 MPa.

Sample	Test	σ_{mean} [MPa]	A [MPa]	f [Hz]	$\epsilon_{1,total}^{inelastic}$[%]	N_{AE}	$A_{AE}^{average}$ [V]
RFD5	Cyclic	85	20	0.014	0.05	469	0.2 ± 0.01
RFD6	Cyclic	85	20	0.0014	0.057	336	0.23 ± 0.012
RFD7	Cyclic	85	20	0.0002	0.06	464	0.24 ± 0.015
RFD8	Cyclic	38	20	0.014	0.031	328	0.14 ± 0.005
RFD10	Cyclic	38	20	0.0014	0.031	310	0.17 ± 0.008
RFD18	Cyclic	38	20	0.0002	0.045	323	0.18 ± 0.007
RFD12	Cyclic	85	5.11	0.014	0.040	–	–
RFD16	Cyclic	85	5.11	0.0014	0.048	–	–
RFD20	Cyclic	85	5.11	0.0002	0.047	–	–
RFD14	Cyclic	38	5.11	0.014	0.016	–	–
RFD17	Cyclic	38	5.11	0.0014	0.01	–	–
RFD21	Cyclic	38	5.11	0.0002	0.027	–	–
RFD9	MS creep	–	–	–	–	–	–

the waveform, like mean axial stress, axial stress amplitude, and frequency (period), is shown in Fig. 4c. It is important to mention that the waveform considers a constant stress rate during loading and unloading periods. Thus, the strain rate varies during these periods.

After designing the cyclic stress scheme, the first step for each test was reaching the desirable confining pressure (σ_3) hydrostatically, which was 10 MPa. During the next phase, axial stress (σ_1) was increased in a deviatoric way to reach the two target mean stress (38 MPa and 85 MPa) which was the mean stress of the waveform. After, the loading software was switched to stress control and used the built-in function to generate triangular waveforms. We applied a total of eight cycles since experiments had to be completed within a day.

In addition to 12 deviatoric tests, one multi-stage creep test was performed to provide the input parameters to model the cyclic test in the brittle regime. During the creep test, the rock sample was subjected to three axial stress (σ_1) levels while keeping the confining pressure (σ_3) constant at 10 MPa. The Multi-step creep test was carried out in axial stress levels of 85 MPa (8 h), 105 MPa (3 h), and 115 MPa (0.65 h). In the next section, the constitutive laws are developed to model the relevant physics undergoing in sandstone.

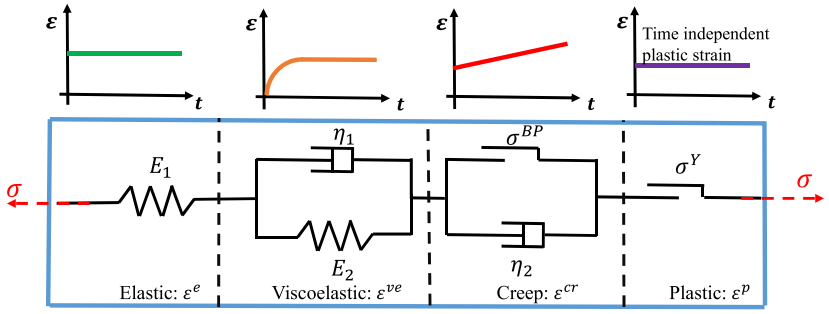

Fig. 5. Schematic illustration of the constitutive model when a constant load is applied.

3. Constitutive law formulation

Based on several experiments and observed physics, different deformation mechanisms were employed, and accordingly, the total strain ($\boldsymbol{\varepsilon}^{\mathrm{t}}$) is split into elastic strain $\boldsymbol{\varepsilon}^{\mathrm{e}}$, plastic strain $\boldsymbol{\varepsilon}^{\mathrm{p}}$, visco-elastic strain $\boldsymbol{\varepsilon}^{\mathrm{ve}}$ and creep strain $\boldsymbol{\varepsilon}^{\mathrm{cr}}$ as

$$\boldsymbol{\varepsilon}^{\mathrm{t}} = \boldsymbol{\varepsilon}^{\mathrm{e}} + \boldsymbol{\varepsilon}^{\mathrm{p}} + \boldsymbol{\varepsilon}^{\mathrm{ve}} + \boldsymbol{\varepsilon}^{\mathrm{cr}}. \tag{1}$$

Schematic illustration of the numerical model is shown in Fig. 5. The elastic strain based on Hooke's law is given by,

$$\boldsymbol{\varepsilon}^{\mathrm{e}} = \frac{q}{E_1}. \tag{2}$$

Here q is the deviatoric stress, E_1 is the elastic Young's modulus. The viscoelastic strain is the time dependent elastic strain which is given by

$$\boldsymbol{\varepsilon}^{\mathrm{ve}} = \frac{q}{E_2}\left(1 - \exp\left(\frac{-E_2}{\eta_1}t\right)\right). \tag{3}$$

Here E_2, η_1 are the Youngs modulus and viscosity of the viscoelastic unit. The creep strain is inelastic strain which is time dependent that is given by

$$\boldsymbol{\varepsilon}^{\mathrm{cr}} = \left(\frac{\sigma_1 - \sigma^{BP}}{\eta_2}\right)\Delta t. \tag{4}$$

Here σ^{BP} is the brittle yield point and η_2 is the viscosity of the brittle creep unit. Finally, the plastic strain is split into two components based on the mechanisms which are given by

$$\boldsymbol{\varepsilon}^{\mathrm{p}} = \boldsymbol{\varepsilon}^{\mathrm{p}}_{\mathrm{compaction}} + \boldsymbol{\varepsilon}^{\mathrm{p}}_{\mathrm{dilation}}. \tag{5}$$

To compute $\boldsymbol{\varepsilon}^{\mathrm{p}}_{\mathrm{compaction}}$ Modified Cam Clay model (MCC) [82] and for $\boldsymbol{\varepsilon}^{\mathrm{p}}_{\mathrm{dilation}}$ hardening softening model was used [75]. Finally, the total strain in the rock is given based on the brittle yield point, i.e.,

$$\boldsymbol{\varepsilon}^{\mathrm{t}} = \begin{cases} \frac{q}{E_1} + \frac{q}{E_2}(1 - \mathrm{e}^{-\frac{E_2}{\eta_1}t}) + f_1(q, \alpha_i) & \sigma_1 < \text{Brittle yield point} \\ \frac{q}{E_1} + \frac{q}{E_2}(1 - \mathrm{e}^{-\frac{E_2}{\eta_1}t}) + \frac{\sigma_1 - \sigma^{BP}}{\eta_2}\Delta t + f_2(q, \beta_i) & \sigma_1 > \text{Brittle yield point} \end{cases} \tag{6}$$

In the following subsections, the plasticity models are elaborated.

3.1. Modified Cam clay model

The MCC model uses a yield surface that determines whether rocks behave in an elastic or plastic behavior. The critical components are shown in the schematic Fig. 6. This model has been used to account for inter-granular cracking, clay crushing, and grain sliding, which takes place below the brittle yield point [42].

In this work, the MCC model is extended to account for cyclic inelastic compaction inspired by the work done by [76]. The yield function is given by

$$f = q^2 - M^2(p(p_c - p)). \tag{7}$$

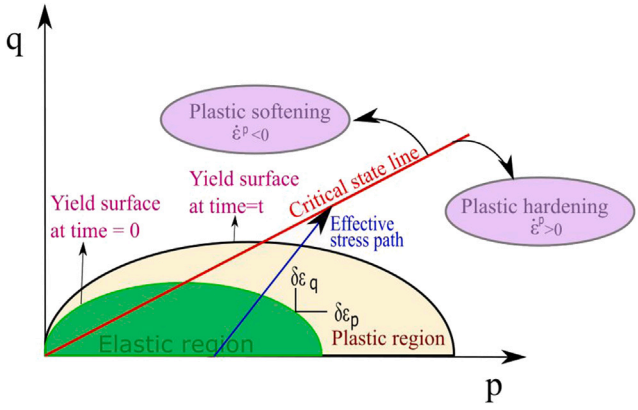

Fig. 6. The schematic diagram of modified cam clay model showing the yield envelopes.

Here M is the slope of the critical state line, p_c is the pre-consolidation pressure, and p is the volumetric stress. The pre-consolidation pressure is expressed as

$$\frac{\delta p_c}{p_c} = \frac{\delta p_l}{p_l}. \tag{8}$$

Here p_l is the loading parameter derived from the yield surface envelope, which is

$$p_l = p + \frac{q}{M}^2\left(\frac{1}{p}\right). \tag{9}$$

The plastic strain is computed from the consistency condition by normalizing the stresses [83,84]. The change in void ratio is given by

$$de = -(1 + e) \times \varepsilon^{\mathrm{p}}_p. \tag{10}$$

The volumetric and deviatoric parts of the incremental plastic strain is given by

$$\begin{bmatrix} \Delta\varepsilon^{\mathrm{p}}_p \\ \Delta\varepsilon^{\mathrm{p}}_q \end{bmatrix} = \Omega \times \begin{bmatrix} M^2 - \eta & 2\eta \\ 2\eta & \frac{2\eta}{M^2 - \eta^2} \end{bmatrix} \times \begin{bmatrix} dp \\ dq \end{bmatrix}. \tag{11}$$

Here,

$$\Omega = \frac{\lambda_{MCC} - \kappa}{(1 + e)p(M^2 + \eta^2)} \tag{12}$$

in which

$$\kappa = \frac{1 + e}{K} \tag{13}$$

and

$$K = \frac{E_{avg}}{3\,(1 - 2\upsilon)}. \tag{14}$$

Furthermore, $\eta = q/p$, $e = \phi/1 - \phi$, ϕ is the porosity, and e is the void ratio. For a detailed derivation, refer to the literature [83,84]. Also,

here dp and dq are the incremental volumetric stress and deviatoric stress, respectively. To account for the cyclic part of the inelastic strains, θ is the parameter employed which accounts for the cyclic element of the MCC model Eq. (8), which is given by

$$\frac{\delta p_c}{p_c} = \theta \frac{\delta p_l}{p_l}. \tag{15}$$

$$p_c^{new} = p_c^{old} \left(\frac{p_l^{max}}{p_c^{old}} \right)^{\theta} \tag{16}$$

So this ensures that a new pre-consolidation parameter p_c^{new} is established cycle after cycle. The evolution of the pre-consolidation parameter is ruled by Eq. (15) and Eq. (16) after integration. This p_c^{new} is lower than p_l^{max} but as the number of cycles increases p_c^{new} tends to the value of p_l^{max}. If θ is equal to 1, the model reduces to the standard MCC. This proposal is inspired by the work of [76], which dealt with the deformation of clays under cyclic loadings. So from this model, plastic strain from $\boldsymbol{\epsilon}^{\mathrm{p}}_{\mathrm{compaction}}$ is computed.

3.2. Hardening softening model

The hardening–softening model is employed to model the plastic strains induced by the fracturing of the grains above the brittle yield point. The model is explained briefly here, and for a deeper understanding, the reader is referred to [75,78]. The model for triaxial conditions ($\sigma_3 = \sigma_2$) is based on Coulomb-Mohrs yield surfaces f_1 and f_2 (Eqs. (17) and (18)), which is given by

$$f_1 = \frac{1}{2}(\sigma_3 - \sigma_1) + \frac{1}{2}(\sigma_1 + \sigma_3)\sin(\phi_f) - c \times \cos(\phi_f) = 0 \tag{17}$$

$$f_2 = \frac{1}{2}(\sigma_2 - \sigma_1) + \frac{1}{2}(\sigma_1 + \sigma_2)\sin(\phi_f) - c \times \cos(\phi_f) = 0. \tag{18}$$

Here c is the cohesion of the rock and ϕ_f is the internal friction angle. Similar surfaces are defined for the plastic potential flow, as can be seen in Eqs. (19) and (20)

$$g_1 = \frac{1}{2}(\sigma_3 - \sigma_1) + \frac{1}{2}(\sigma_1 + \sigma_3)\sin(\psi) + \text{constant} \tag{19}$$

$$g_2 = \frac{1}{2}(\sigma_2 - \sigma_1) + \frac{1}{2}(\sigma_1 + \sigma_2)\sin(\psi) + \text{constant}. \tag{20}$$

Here ψ is the dilation angle. These plastic potential functions (g_1 and g_2) are responsible for the magnitude of the plastic strain increments $\dot{\boldsymbol{\epsilon}}^p$, as can be seen in the general plasticity rule depicted by Eq. (21) as well as in Eqs. (22) and (23) for axial and volumetric plastic strains respectively. The rate of plastic strain is given by

$$\dot{\boldsymbol{\epsilon}}^p = \lambda_1 \frac{\partial g_1}{\partial \boldsymbol{\sigma}} + \lambda_2 \frac{\partial g_2}{\partial \boldsymbol{\sigma}} \tag{21}$$

$$\dot{\epsilon}_1^p = \frac{1}{2}(\lambda_1 + \lambda_2)(-1 + \sin(\psi)) \tag{22}$$

$$\dot{\epsilon}_v^p = (\lambda_1 + \lambda_2)\sin(\psi). \tag{23}$$

The plastic multipliers are computed using the below expressions which are obtained from [78], given by

$$\lambda_1 = \frac{\mu_4 \left(\frac{\partial f_1}{\partial \boldsymbol{\sigma}}\right)^T \mathbb{D}\dot{\boldsymbol{\epsilon}} - \mu_2 \left(\frac{\partial f_2}{\partial \boldsymbol{\sigma}}\right)^T \mathbb{D}\dot{\boldsymbol{\epsilon}}}{\mu_1\mu_4 - \mu_2\mu_3} \tag{24}$$

$$\lambda_2 = \frac{\mu_1 \left(\frac{\partial f_2}{\partial \boldsymbol{\sigma}}\right)^T \mathbb{D}\dot{\boldsymbol{\epsilon}} - \mu_3 \left(\frac{\partial f_1}{\partial \boldsymbol{\sigma}}\right)^T \mathbb{D}\dot{\boldsymbol{\epsilon}}}{\mu_1\mu_4 - \mu_2\mu_3}. \tag{25}$$

Where μ_1, μ_2, μ_3 and μ_4 are define as:

$$\mu_1 = \left(-\frac{\partial f_1}{\partial \bar{\epsilon}^p}\frac{\partial \bar{\epsilon}^p}{\partial \boldsymbol{\epsilon}^p} + \mathbb{D}\frac{\partial f_1}{\partial \boldsymbol{\sigma}} \right)^T \frac{\partial g_1}{\partial \boldsymbol{\sigma}} \tag{26}$$

$$\mu_2 = \left(-\frac{\partial f_1}{\partial \bar{\epsilon}^p}\frac{\partial \bar{\epsilon}^p}{\partial \boldsymbol{\epsilon}^p} + \mathbb{D}\frac{\partial f_1}{\partial \boldsymbol{\sigma}} \right)^T \frac{\partial g_2}{\partial \boldsymbol{\sigma}} \tag{27}$$

$$\mu_3 = \left(-\frac{\partial f_2}{\partial \bar{\epsilon}^p}\frac{\partial \bar{\epsilon}^p}{\partial \boldsymbol{\epsilon}^p} + \mathbb{D}\frac{\partial f_2}{\partial \boldsymbol{\sigma}} \right)^T \frac{\partial g_1}{\partial \boldsymbol{\sigma}} \tag{28}$$

$$\mu_4 = \left(-\frac{\partial f_2}{\partial \bar{\epsilon}^p}\frac{\partial \bar{\epsilon}^p}{\partial \boldsymbol{\epsilon}^p} + \mathbb{D}\frac{\partial f_2}{\partial \boldsymbol{\sigma}} \right)^T \frac{\partial g_2}{\partial \boldsymbol{\sigma}}. \tag{29}$$

$\mathbb{D}$ is the elasticity matrix, and the hardening parameter $\bar{\epsilon}^p$ is given by

$$\bar{\epsilon}^p = \int \sqrt{\frac{2}{3}(\dot{\epsilon}_1^p\dot{\epsilon}_1^p + \dot{\epsilon}_2^p\dot{\epsilon}_2^p + \dot{\epsilon}_3^p\dot{\epsilon}_3^p)}dt. \tag{30}$$

The expressions for the above parameters are elaborated in Appendix Appendix. Dilation-based plastic strain is computed from this model.

Next section, we observe the experimental results obtained from imposing cyclic loading on sandstone.

4. Experimental results

4.1. Behavior of stress and strain

The total inelastic strain was computed by subtracting the strain of the initial loading from the strain at the final unloading at a referential stress of 15 MPa as shown by Eq. (31) and (Fig. 7(b)). The stress was not decreased to exactly the confining pressure (10 MPa) to avoid damage to the cell's silicon jacket. The cumulative apparent inelastic axial strain over the cycle is estimated by subtracting the axial strain at the end of every cycle minus the strain at the beginning of the first cycle (Eq. (32) and Fig. 7(b)). All strains were measured at minimum axial stress of the cyclic test. This inelastic strain is considered apparent because it is affected by the time-dependent deformation of the rock.

$$\boldsymbol{\epsilon}^{\text{inelastic}}_{1,total} = \boldsymbol{\epsilon}^2_{1f} - \boldsymbol{\epsilon}^1_{1in} \tag{31}$$

$$\boldsymbol{\epsilon}^{\text{inelastic}}_{1,apparent} = \boldsymbol{\epsilon}^4_{1f} - \boldsymbol{\epsilon}^3_{1in} \tag{32}$$

Fig. 7(a) shows the imposed stress and strain behavior against time for the test with the lowest frequency (0.0002 Hz) and larger amplitude (20 MPa) in the brittle regime. In this figure, it can be seen that the axial strain ($\boldsymbol{\epsilon}_1$) increases from one cycle to the other, where the peaks and valleys show a clear rising trend. In the stress–strain curve (Fig. 7(b)) the final unloading curve has a concave shape, and the apparent elastic strain is larger than the total inelastic strain, which can be due to the visco-elasticity. The total and the apparent inelastic strain were calculated for all 12 tests to investigate the effect of different stress regimes, frequencies, and amplitudes on inelastic deformation.

The total inelastic strain after eight cycles was estimated following Eq. (31) and the results are shown in Fig. 8. As expected, there are inelastic strains when cyclic loading is applied in the brittle regime ($\boldsymbol{\sigma}_{mean1}$ > brittle yield point). In the fully elastic regime, however, there are also inelastic deformations ($\boldsymbol{\sigma}_{mean1}$ < brittle yield point). Inelastic strains in the brittle regime are larger than in the elastic regime. Stress amplitude also has an impact on inelastic strain in both regimes. The larger the amplitude, the larger the inelastic strain. Frequency affects the total inelastic strain in both regimes. The effect of frequency is more pronounced in the elastic regime, and by reducing the frequency, total inelastic strain increases.

4.2. Cumulative apparent inelastic strain over cycles

Ideally, inelastic strain should be measured at deviatoric stress equal to zero. Nevertheless, the apparent inelastic strain is used as a qualitative estimation to understand the evolution of inelastic strain per cycle (Eq. (32)). Fig. 9 shows typical results obtained in every test. The main observation is that the largest apparent inelastic strain occurs in the first cycle. For the following cycles, the rate of inelastic strain per cycle decreased. However, the rate of the decrease in inelastic strain for the test performed in an elastic regime is higher than the test in the brittle regime and approaching zero Fig. 9(b).

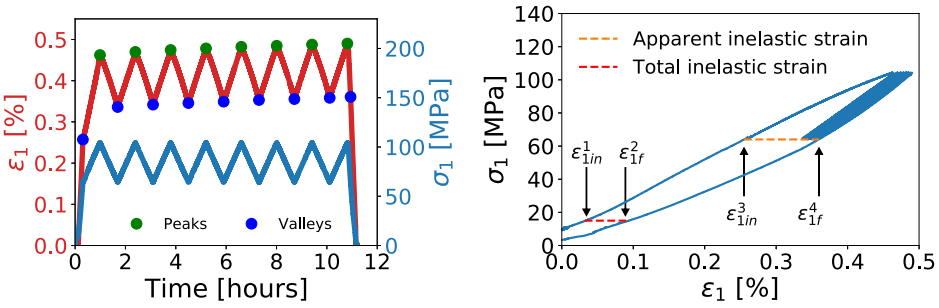

(a) (b)

Fig. 7. Imposed cyclic stress and strain response during the time: (a). Evolution of peaks and valleys for the strain, (b). Calculation of total and apparent inelastic strain.

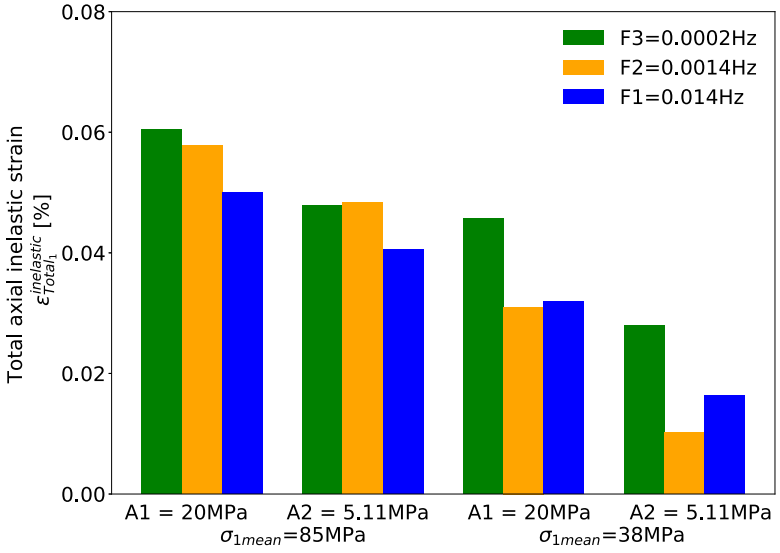

Fig. 8. Effet of stress regime, amplitude, and frequency on total inelastic deformation at the end of the experiments.

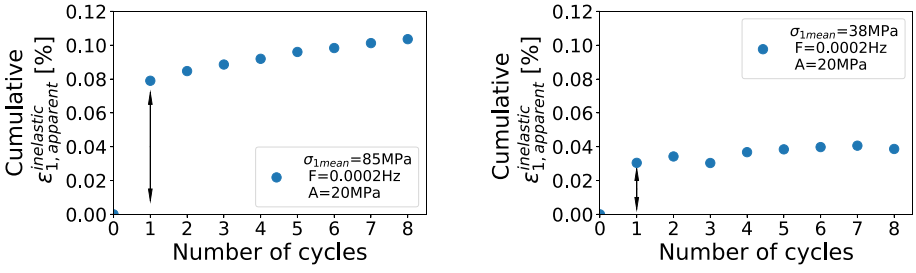

(a) σ_{mean} = 85 MPa (b) σ_{mean} = 38 MPa

Fig. 9. Apparent inelastic axial strain versus the number of cycles in both studied regime: (a) Brittle regime, and (b) the elastic regime, for the lowest frequency $f = 0.0002$ Hz and maximum amplitude. Arrows indicate the inelastic deformation from the first cycle.

To complement the analysis, the results of the cumulative apparent inelastic strain of the 12 tests were plotted for the same amplitude and deformation regime as shown in Figs. 10 and 11. The apparent inelastic strain of the first cycle was removed to improve the comparison and focus on strain evolution over the cycles. Figs. 10(a) and 10(b) show that deformation in the brittle regime is time-dependent and inelastic strain increases per cycle. Reducing the frequency within the brittle zone increases the inelastic strain. This time-dependent deformation can be caused by visco-elastic and/or brittle creep behavior. For the tests in the elastic regime (Figs. 11(a) and 11(b)), there is no time-dependent deformation, and all the inelastic strains approach zero by increasing the number of cycles. According to Figs. 10 and 11, by reducing the amplitude of cycles, the magnitude of the inelastic strain decrease for both stress regimes. The effect of frequency within the elastic regime is not clear, which can be due to the instability or sensitivity of the machine to small deformations (Figs. 11(a) and 11(b)).

4.3. Acoustic emissions and inelastic strain

The AE events were recorded only for the tests corresponding to the maximum stress amplitude (20 MPa). Different parameters from the AE technique, such as AE energy, amplitude, and the number of AE, can be used to interpret failure and deformation mechanisms. As shown in Fig. 12(a), the AE amplitude was plotted together with imposed axial stress versus time. AE events were recorded early in the first

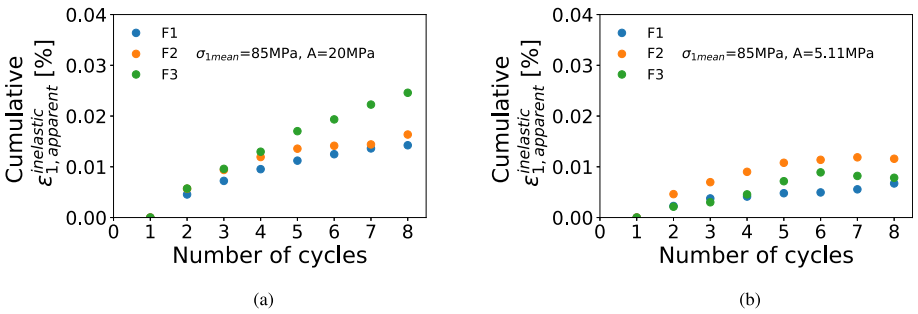

Fig. 10. Comparison of cumulative apparent inelastic strain evolution after removing the first cycle for the different tested frequencies (F1 = 0.014 Hz, F2 = 0.0014 Hz, F3 = 0.0002 Hz) within the brittle regime: (a) Results with amplitude of 20 MPa, (b) Results with amplitude of 5.11 MPa.

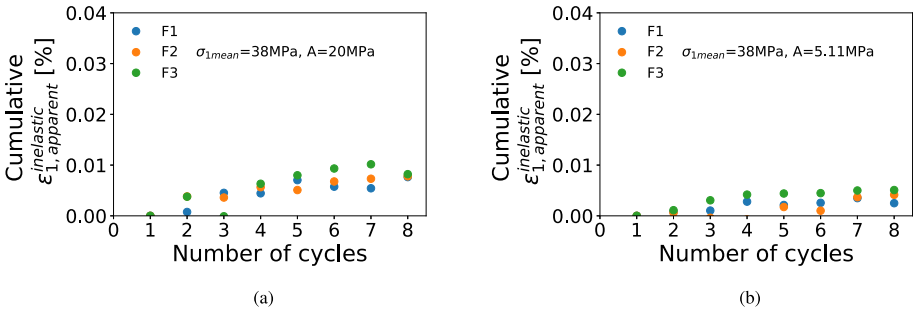

Fig. 11. Comparison of cumulative apparent inelastic strain evolution after removing the first cycle for the different tested frequencies (F1 = 0.014 Hz, F2 = 0.0014 Hz, F3 = 0.0002 Hz) within the elastic regime: Results with amplitude of 20 MPa, (b) Results with amplitude of 5.11 MPa.

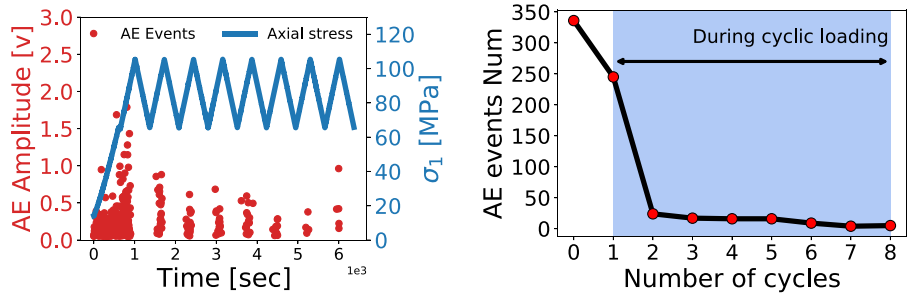

Fig. 12. The results of acoustic emissions: (a) AE amplitude together with axial stress versus time, (b) Evolution of the number of AE events per cycle. The result is for the test with medium frequency (0.0014 Hz) and larger amplitude (20 MPa) in the brittle regime.

loading interval at axial stress slightly higher than the confining stress. After starting the cyclic loading, the maximum acoustic intensity and the number of events were recorded in the first cycle. In general, by increasing the number of cycles, the number of AE and amplitude decreased (Fig. 12(b)).

Results concerning the effect of the deformation regime and frequency on the AE amplitude and number of AE events are shown in Fig. 13. In terms of AE amplitude, the average AE amplitude for the tests in the brittle regime is higher than the average AE amplitude for the tests in the elastic regime (Table 1).

This was an anticipated result; micro-fracturing in the brittle regime is expected to release more elastic energy than any other mechanism presented at a stress lower than the brittle yield point. In addition to AE amplitude, the number of generated AE during the first cycle and the total number of AE events in the brittle regime is more than in the elastic regime. The total number of AE events for the elastic regime is similar for the three tested frequencies (Table 1).

Acoustic emissions are, in most cases, an indicator of inelastic strains, as mentioned by [85]. There is an interesting and similar observation between AE and inelastic strain per cycle. In essence, the maximum number of AE events and major inelastic strain were observed during the first cycle and then decreased by increasing the number of cycles (Figs. 9 and 13). Fig. 14 indicates a strong linear correlation between a cumulative number of AE events and cumulative apparent inelastic strain. The linear regression slope for samples subjected to the brittle regime is more than those subjected to the elastic regime (Fig. 14(a)). Besides, a change in frequency within the brittle regime influences the correlation slope; however, there is no significant influence of frequency change within the elastic regime.

4.4. Discussion and interpretation of experimental results

The possible reasons behind the obtained results regarding deformation and AE characteristics in both elastic and brittle regimes can be discussed separately. As expected, inelastic strains and AE were recorded when tests were carried out in the brittle regime (axial stresses higher than brittle yield point). When the maximum axial stress is higher than the brittle yield point, the critical and/or sub-critical microcracks are induced in the quartz grains, leading to irreversible changes in the rock microstructure and the release of elastic waves [37,41]. An

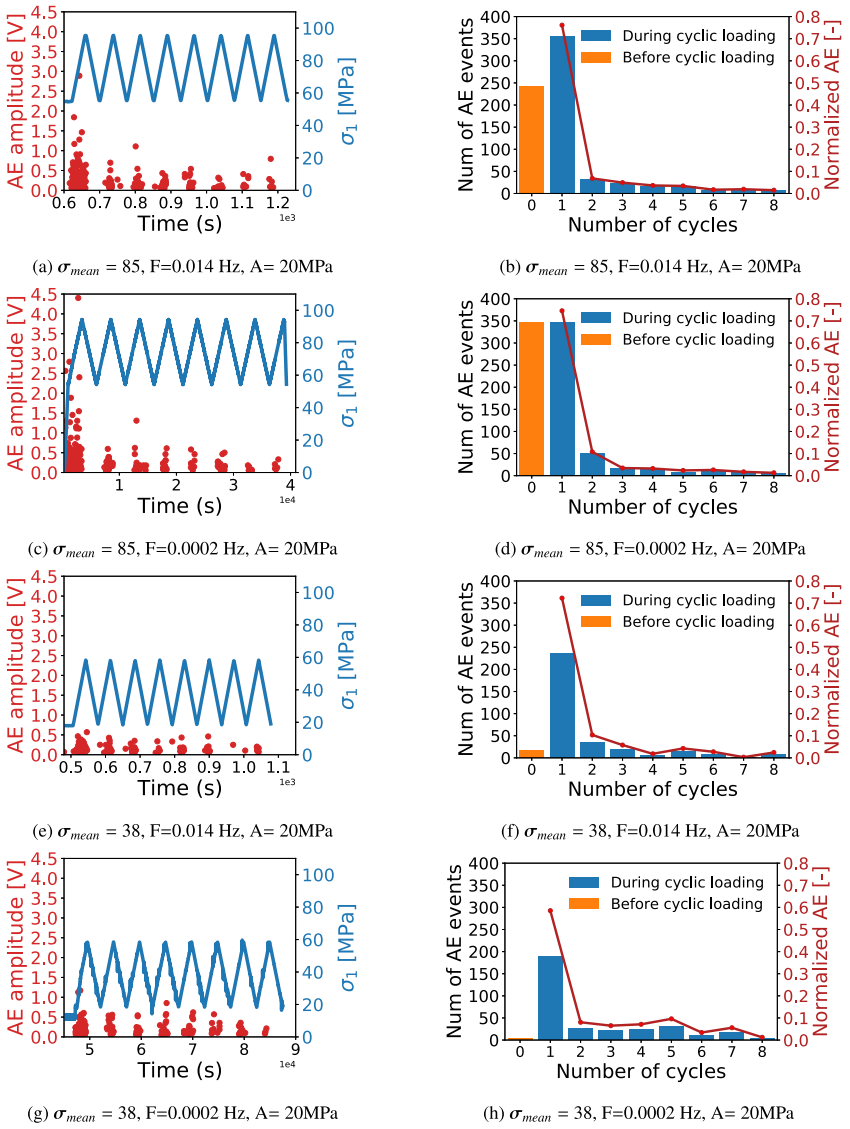

(a) σ_{mean} = 85, F=0.014 Hz, A= 20MPa (b) σ_{mean} = 85, F=0.014 Hz, A= 20MPa

(c) σ_{mean} = 85, F=0.0002 Hz, A= 20MPa (d) σ_{mean} = 85, F=0.0002 Hz, A= 20MPa

(e) σ_{mean} = 38, F=0.014 Hz, A= 20MPa (f) σ_{mean} = 38, F=0.014 Hz, A= 20MPa

(g) σ_{mean} = 38, F=0.0002 Hz, A= 20MPa (h) σ_{mean} = 38, F=0.0002 Hz, A= 20MPa

Fig. 13. Comparison of the AE event numbers and AE amplitude for tests in brittle (a, b, c, and d) and elastic (e, f, g, and h) regimes at different frequencies and fixed amplitude of 20 MPa. Figures a, c, e, and g show the AE amplitude together with axial stress versus time, and figures b, d, f, and h illustrate the evolution of AE event numbers per cycle.

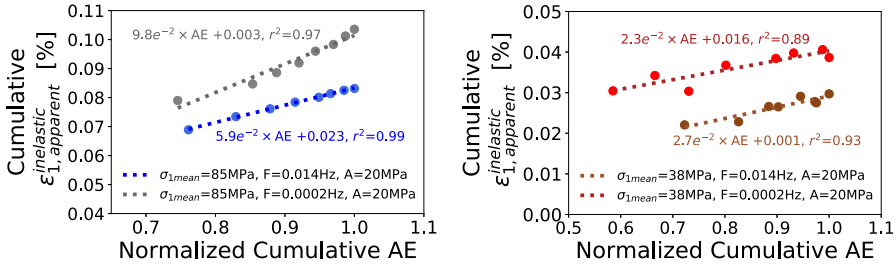

(a) (b)

Fig. 14. Cross plot of cumulative AE vs cumulative inelastic strain. (a) The brittle regime, (b) The elastic regime.

increase in the amplitude of cycles can create high-stress concentrations between grains, leading to more inter-granular and intra-granular cracks being induced. For the Red Felser sandstone, it is clear that the rock can experience time-dependent inelastic deformations when the stress is above the brittle yield point. This was proven by the results of the creep tests (see Fig. 19) and by the effect of frequency on apparent inelastic strain during deviatoric cyclic tests (see Fig. 10). This deformation mechanism is called brittle creep [37]. Therefore, using low frequency and high amplitude cycles induces more inelastic deformations (Fig. 8).

Interestingly, inelastic strain and AE were also recorded in the elastic regime (axial stresses lower than brittle yield point), where only elastic strains are usually expected. Inelastic deformations at low-stress levels for sandstone have also been reported by [42,86]. From the

Table 2
Model parameters used to reproduce experimental multistage creep test 2. These parameters will remain constant during modeling brittle cyclic tests, except for the viscosity of the visco-elastic unit, which changes depending on the frequency of the cyclic load.

Physics	Value	Value	Value	Value
Viscoelasticity	E_1 = 46 GPa	E_2 = 49 GPa	η_1 = 13e3 GPa s	ν = 0.125
MCC	M = 2.35 [42]	λ_{MCC} = 1.2e−4	p_c^0 = 10.1 MPa	ϕ = 0.2056
HS model	E_{avg} = 23.7	c = 22 MPa	$\phi_{friction}$ = 34.5	ε_f = 0.0015
Brittle creep	η_2 = 18e5 GPa s	σ^{BP} = 81 GPa s		

micro-structural point of view, inelastic strains in sandstones below the brittle yield point have been interpreted as irreversible rock compaction caused by crushing and slip of clay layers plus inter-granular cracking [42,45]. Red Felser sandstone comprises low volumetric proportions of clay and orthoclase grains that could crush or brake at stress levels lower than the onset for intra-granular cracking of quartz grains. Regarding the cyclic inelastic strains, it has been related to the irreversible closure of induced and existing cracks [87].

For the same stress amplitude, the AE amplitude and the total number of AE differ between the two regimes, as shown in Fig. 13, Fig. 14, and Table 1. This indicates the different mechanisms that are taking place. For instance, micro-cracking of quartz grains that takes place above the brittle yield point is expected to release more energy than inter-granular cracking, clay crushing, or grain sliding, which are the possible mechanisms below the brittle yield point.

Based on the observations from the experiments, the comparison between the developed constitutive model in Section 3 with experimental results are elaborated.

5. Modeling results

5.1. Below brittle yield point

Firstly, the constitutive laws are calibrated with the first cycle and further they are compared with the experimental results in the remaining cycles. From Fig. 14, it was found that the apparent inelastic strain (viscoelastic + inelastic) is directly proportional to the AE. Based on this observation, the number of recorded AE events for every cycle and only the estimate of inelastic strain from AE events is correlated by using a direct proportionality. Using normalized AE as presented in Fig. 13, the estimate of inelastic strain for each cycle is given by

$$\varepsilon_1^{Inelastic,i} = \frac{AE_i}{AE_{\text{Total}}} \times \varepsilon_{Total}^{Inelastic}. \tag{33}$$

Here AE_{Total} is the total number of AE events during stress cycling, AE_i is the number of AE events recorded at each cycle 'i' and $\varepsilon_{Total}^{Inelastic}$ is the total inelastic strain from the experiments. Using the superposition principle [88], the cyclic variation of 'q' with a deviatoric stress stepping scheme was employed. Young's modulus of the rock (elastic and viscoelastic) was initially calibrated with the first cycle of each experiment. Then, the MCC model parameters were fine-tuned using the inelastic strain from the first cycle. Using these parameters, the experimental results are compared with the analytical solutions.

Table 3 shows the parameters employed for the three frequencies at an amplitude of 20 MPa. Figs. 15(a) and 15(c) show the variation of axial strain with time for experimental and modeling results for frequencies 0.0014 Hz and 0.0002 Hz. The modeling results showed a very good fit compared to experimental results for all the frequencies. The difference between the total inelastic strain for experimental and modeling results is also presented in the last column of Table 3. The highest difference between them is around 7% for the lowest frequency.

Figs. 15(b) and 15(d) show the variation of inelastic strain with time obtained from the MCC model, which is compared with the inelastic strain estimated using the number of events of AE (Eq. (33)) for the same frequencies. It can be seen that the MCC model is successful in capturing the inelastic strain cycle after cycle. The increase in inelastic strain for every cycle which is based on AE, follows a similar trend as the cyclic MCC model and quantitatively captures well with the experiments.

The yield surface evolution for different input loading cycles is shown in Fig. 16. As the number of cycles increase, the yield surface slowly evolves to reach the maximum-sized final yield envelope. The plasticity model employed here with the parameters calibrated from the first cycle showed maximum decrease in 0.2% porosity at the end of the experiment. Though the decrease in porosity was not measured experimentally, previously few researchers have shown the decrease in porosity of sandstone under triaxial loading [42]. In the energy storage perspective, porosity reduction implies the reduction in storage capacity of the subsurface reservoirs caused due to accumulated inelastic deformation. From the Table 3, it can also be seen that the parameters λ_{MCC} and viscosity η_1 are increasing with decreasing frequency. The rest of the parameters, such as θ, p_c pre-consolidation pressure, and E_{avg} are constant for all the frequencies. The viscosity of the rock increases with decreasing frequency of the applied load.

In the context of energy storage and upscaling the lab to energy storage conditions, viscoelastic frequency will become a key parameter when compared to rest of the material parameters used in the constitutive models. Viscoelastic frequency is a parameter directly influenced by cyclic loading frequency. It is interpreted that this viscosity could also be a function of strain rate as presented for the creep viscosity [89,90]. Thus, as frequency decreases, the mean strain rate decreases, causing the viscosity to increase, which suggests a strain rate thinning-like behavior. To further support this, Fig. 17 shows the viscosity variation with the loading frequency. Authors [91], model sandstone-based Bergermeer gas field storage sites with the viscoelastic model. The viscosity used by them to compare the uplift with GPS stations was around 1e8 GPa s. Using this as evidence, it can be said that depending on the frequency of cyclic loading viscosity of the viscoelastic model needs to be modified accordingly.

5.2. Above brittle yield point

Here we employ the hardening softening model, and brittle creep additionally because the loading zone is above the brittle yield point. So the first step is defining the parameters of these two models, which are considered independent of the frequency of cyclic loading. For the calibration of the hardening–softening model, the range for cohesion and friction angle was established. This was done through monotonic test results for Red Felser sandstone at different confining pressures, as shown in figure Fig. 18. It can be seen that cohesion could range between 12 MPa and 32 MPa while the internal friction angle could be between 25° and 48° for σ_3 = 10 MPa.

The hardening softening (HS) model was further calibrated with the first loading cycle of the test case $\sigma_{mean}1/F3/A1$. This was done using the trial and error method. Next, the creep model was calibrated against the Multistage creep test. Thus, initial calibration of the viscoelastic and MCC model parameters also occurred. Fig. 19(a) shows that it was possible to reproduce the strain of all the loading steps. The imposed axial load (σ_1) is shown in Fig. 19(a). In this test case, the model comprises all the models (elastic, viscoelastic, creep, MCC, and HS model). Table 2 shows all the parameters obtained from fitting the experimental data for only the multistage creep test. The critical state line 'M' slope was taken from [42].

Table 3
Model input parameters and difference in total inelastic strain between the model and lab measurements for tests in the 'elastic regime' (σ_{mean2} = 38 MPa) and amplitude $A1$ of 20 MPa.

Test	f [Hz]	λ_{MCC}	θ	η_1 GPa s	E_{avg}	p_c	$\epsilon^{inelastic}$ Model/Lab
$\sigma_{mean2}/F1/A1$	F1 = 0.014	1.50e−04	0.005	250	23.3	10	0.0314/0.0319
$\sigma_{mean2}/F2/A1$	F2 = 0.0014	1.85e−04	0.005	1900	23.3	10	0.030/0.031
$\sigma_{mean2}/F3/A1$	F3 = 0.0002	2.30e−04	0.005	13000	23.3	10	0.042/0.045

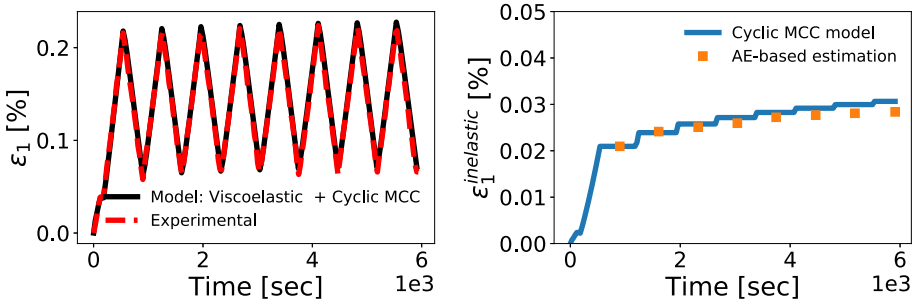

(a) Axial strain v/s time for f = 0.0014 Hz

(b) Inelastic strain v/s time for f = 0.0014 Hz

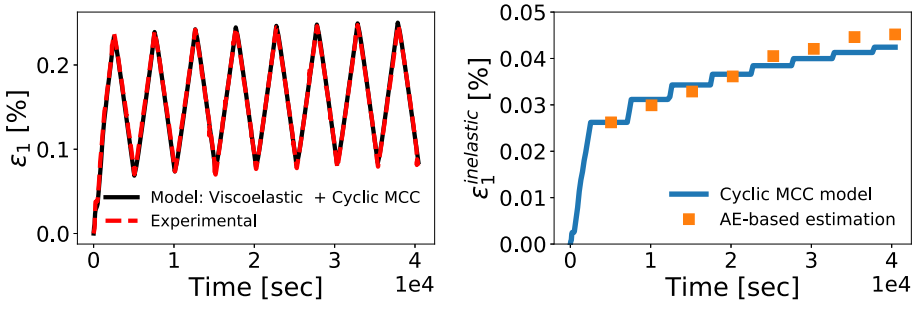

(c) Axial strain v/s time for f = 0.0002 Hz

(d) Inelastic strain v/s time for f = 0.0002 Hz

Fig. 15. Below brittle yield point: The above figures show the variation of axial strain with time (15(a), 15(c)). The respective inelastic strain with time is shown in (15(b), 15(d)).

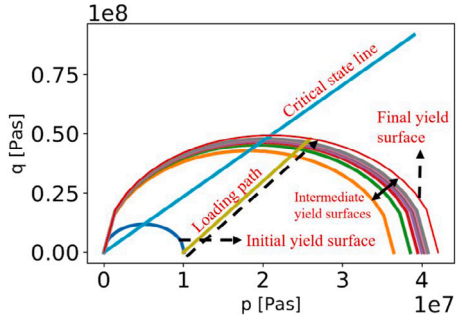

Fig. 16. Illustration of the evolving yield envelope for every cycle of the rock using the MCC.

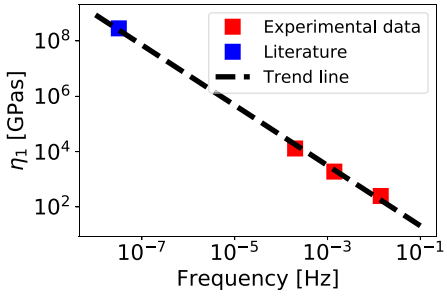

Fig. 17. The variation of viscosity of rocks with the frequency of the cyclic loading. The field scale relevant data is from the literature [91] (Blue square). (For interpretation of the references to color in this figure legend, the reader is referred to the web version of this article.)

Fig. 19(b) shows the variation of deviatoric stress with axial strain for the multi-stage creep test. The red and green double-headed arrows highlight the creep (visco-elastic + inelastic) strains and only inelastic strains, respectively. Using this, the viscoelastic and inelastic strain contributions could be identified, which helps calibrate the constitutive model.

Finally, the deviatoric cyclic tests performed in the brittle regime were compared with the proposed model (Eq. (6)) after the calibration as shown in Fig. 20. Figs. 20(a) and 20(c) show the variation of axial strain with time for two frequencies f = 0.0014 Hz and f = 0.0002 Hz. The inelastic strain contributions with the time of the three models are shown in Fig. 20(b) and Fig. 20(d), respectively, for the same two frequencies. It can be seen that brittle creep plays an important

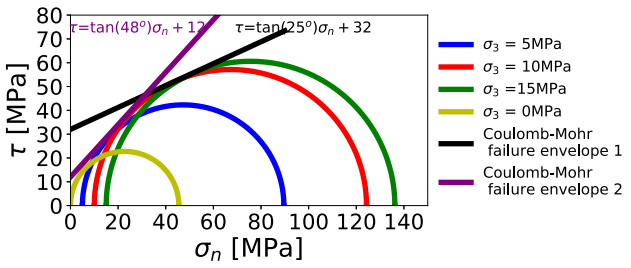

Fig. 18. The figure shows the variation of shear stress with normal stress (failure envelop) with the equation of the Mohr-coulomb failure criteria can be seen.

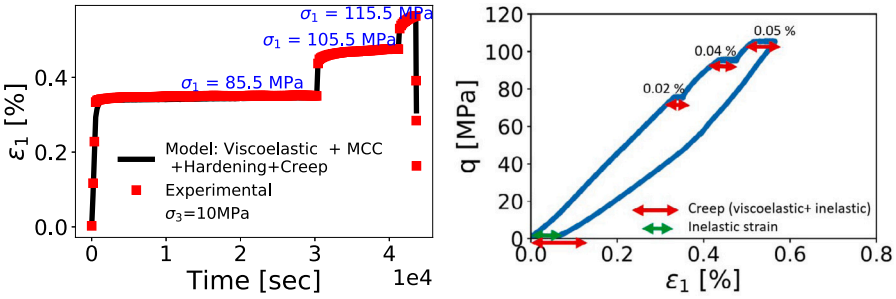

(a) Strain v/s time (b) Stress v/s strain

Fig. 19. The figure shows the variation of strain with time for the imposed stress (σ_1) as shown in Fig. 19(a) for a multi-stage creep test. The creep strain (viscoelastic+inelastic) and the inelastic strains are highlighted in red and green arrows, respectively as shown in Fig. 19(b). (For interpretation of the references to color in this figure legend, the reader is referred to the web version of this article.)

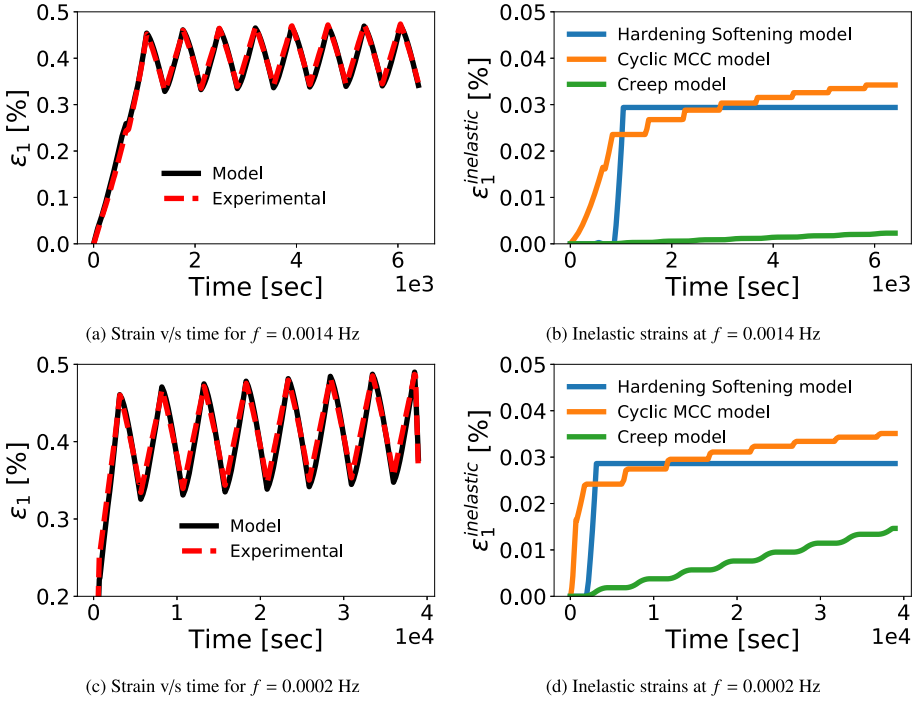

(a) Strain v/s time for f = 0.0014 Hz (b) Inelastic strains at f = 0.0014 Hz

(c) Strain v/s time for f = 0.0002 Hz (d) Inelastic strains at f = 0.0002 Hz

Fig. 20. Above brittle yield point: The variation of axial strain with time and inelastic strains with time for all the frequencies are shown. The constitutive model comprises elastic, viscoelastic, creep, MCC, and HS model.

Table 4
Model parameters: θ and visco-elastic viscosity η_1 against frequency for tests in the brittle regime. It is also mentioned the difference in total inelastic strain between the model and lab measurements. $F1 > F2 > F3$. Here σ_{mean1} = 85 MPa and $A1$ = 20 MPa.

Test	Frequency [Hz]	θ	η_1 [Gpa s]	Eavg. [GPa]	$\varepsilon^{inelastic}$ [%] Model/Lab
$\sigma_{mean1}/F1/A1$	F1 = 0.014	0.005	650	21.8	0.05/0.07
$\sigma_{mean1}/F2/A1$	F2 = 0.004	0.005	7800	21.8	0.058/0.065
$\sigma_{mean1}/F3/A1$	F3 = 0.0002	0.005	40000	21.8	0.0604/0.079

role as the frequency decreases because there is more time for this type of deformation to become significant. In addition, cyclic plasticity was required to reproduce the experimental results of all the tests at the amplitude of 20 MPa (A1). Cyclic plasticity was more significant for high-frequency tests because of the negligible creep contribution Fig. 20(b). The results for f = 0.014 Hz also showed a good fit for both below the yield point and above the yield point regimes.

Similar to the previous tests conducted below the brittle yield point, the viscoelastic viscosity had to be increased when the frequency of loading of cyclic tests was reduced, as shown in Table 4. Also, the viscosity in these test cases is consistently higher than the tests conducted in the elastic regime. The difference between the total inelastic strain for experimental and modeling results is also presented in the last column of Table 4. Due to the higher number of parameters involved

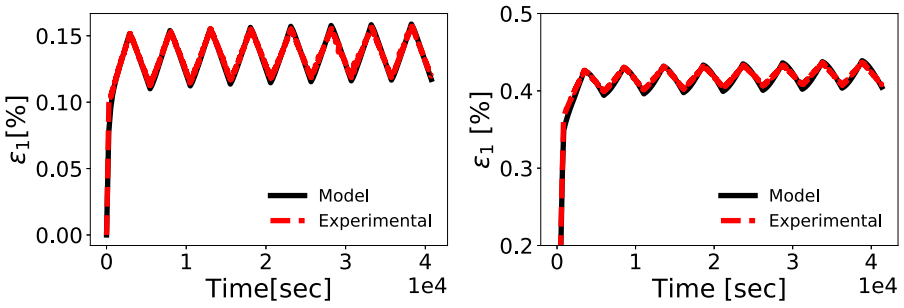

(a) σ_{mean2} = 38 MPa and A = 5.11 MPa (b) σ_{mean1} = 85 MPa and A = 5.11 MPa

Fig. 21. The variation of axial strains with time for lower amplitude A2 (A = 5.11 MPa), lowest frequency f = 0.0002 Hz and different mean stresses.

Table 5
Model parameters: θ and visco-elastic viscosity η_1 against frequency for tests in the brittle regime. The below parameters are for the amplitudes $A2$ = 5.11 MPa for both the means stresses at the lowest frequency.

Test	Frequency [Hz]	θ	η_1 [Gpa s]	Eavg. [GPa]
$\sigma_{mean1}/F3/A2$	F3 = 0.0002	0.005	13000	20.9
$\sigma_{mean2}/F3/A2$	F3 = 0.0002	0.005	45000	23.11

from constitutive models, this difference is higher when compared to the previous section of below brittle yield point. No powerful optimization algorithms were employed, and lastly, the cyclicity part of dilation-based plasticity constitutive law was not accounted for. They are beyond the scope of this work.

In the subsurface energy storage perspective, considering much higher time scales with very low frequencies (max. 1e−6 Hz), creep deformation can become the most significant inelastic mechanism compared to the rest. Visco-elasticity will become critical during the injection and production of the reservoir to ensure that the strain-thinning behavior of sandstone rocks is considered.

Next, the effect of amplitude of cyclic loading for different regimes of stresses can be seen in Fig. 21. Figs. 21(a) and 21(b) show the variation of axial strain with time for mean stresses 38 MPa and 85 MPa, respectively. The parameters used in this amplitude are presented in Table 5.

Here we see that the constitutive model fits the experimental data even for lower amplitudes. The Young's modulus (Eavg) is slightly different for mean stress 1 and 2, irrespective of amplitude and frequency. However, we did not observe any trend in the variation of Eavg depending on the stress regimes. The values of the parameters involved in constitutive models can slightly change if powerful optimization algorithms are employed. However, we expect the qualitative behavior of sandstone rock based on the above operating conditions would remain the same.

6. Conclusion

We conducted an extensive experimental and modeling analysis for Red Felser sandstone rock subjected to cyclic loading. Three different frequencies, two amplitudes, and two different stress regimes of cyclic loading on sandstone were studied using axial strain and acoustic emissions. Further, a constitutive model was developed based on literature, which is specifically suitable for sandstone rocks but could be extended for other porous rocks. Major conclusions are

- The inelastic deformations occurred at stress conditions above and below the brittle yield point (onset of dilatant cracking). The inelastic strain per cycle decreased as the number of cycles increased. Therefore, fatigue was not registered within the number of cycles tested.
- The cyclic inelastic deformations were affected by the mean stress, amplitude, and frequency of the stress waveform imposed during testing. On the one hand, the higher the mean stress or amplitude, the higher the total inelastic strains. On the other hand, the lower the frequency, the higher the total inelastic strain.
- There is a strong correlation between the cumulative number of AE vs. cumulative apparent inelastic strain. They both decrease by increasing the number of cycles.
- The proposed constitutive model based on governing physics showed a very good fit with the experimental results. The viscosity of the rock was found to be the most critical parameter which needs to be accounted for depending on the frequency of the cyclic loading.
- The cyclic MCC model captures the estimation of inelastic deformation based on the increase in the number of AE events happening cycle after cycle.

CRediT authorship contribution statement

Milad Naderloo: Conceptualization, Methodology, Experiments, Writing – original draft, Editing. **Kishan Ramesh Kumar:** Conceptualization, Methodology, Modelling, Writing – original draft, Editing. **Edgar Hernandez:** Conceptualization, Methodology, Experiments, Modeling. **Hadi Hajibeygi:** Conceptualization, Supervision, Grant acquiring, Writing – review & editing. **Auke Barnhoorn:** Conceptualization, Supervision, Grant acquiring, Writing – review & editing.

Declaration of competing interest

The authors declare that they have no known competing financial interests or personal relationships that could have appeared to influence the work reported in this paper.

Data availability

Data will be made available on request

Acknowledgments

The financial support of NWO-TTW ViDi grant (project ADMIRE 17509) is acknowledged. The authors would like to thank all the members of ADMIRE project members at TU Delft, for the fruitful discussions. Especial thanks to the technical team in the rock deformation lab at the Technical University of Delft. This research was (partially) funded by NWO Science domain (NWO-ENW), project DEEP.NL.2018.048.

Appendix

This section elaborates on the computation of the plastic strains using hardening softening model, caused due to dilation. The variables used to calculate the plastic multipliers in Eqs. (24) and (25) for the hardening–softening plastic model are elaborated. The nomenclature is from [75] will be used.

The stress–strain rate elastic relationship is expressed in matrix and abbreviated forms as follows:

$$\begin{pmatrix} \dot{\sigma_{1,1}} \\ \dot{\sigma_{2,2}} \\ \dot{\sigma_{1,2}} \\ \dot{\sigma_{3,3}} \end{pmatrix} = \begin{pmatrix} \lambda+2\mu & \lambda & \lambda & 0 \\ \lambda & \lambda+2\mu & \lambda & 0 \\ 0 & 0 & 0 & \mu \\ \lambda & \lambda & \lambda+2\mu & 0 \end{pmatrix} \begin{pmatrix} \dot{\varepsilon_{1,1}} \\ \dot{\varepsilon_{2,2}} \\ \dot{\varepsilon_{1,2}} \\ \dot{\varepsilon_{3,3}} \end{pmatrix} \tag{34}$$

$$\dot{\boldsymbol{\sigma}} = \mathbb{D}\dot{\boldsymbol{\epsilon}}^{elastic} \tag{35}$$

The variation of the yield and potential flow surfaces with respect to stress are vectors:

$$\frac{\partial f_1}{\partial \boldsymbol{\sigma}}^T = [-\frac{1}{2} + \frac{1}{2}sin(\phi^*_{friction}), 0, 0, \frac{1}{2} + \frac{1}{2}sin(\phi^*_f)] \tag{36}$$

$$\frac{\partial f_2}{\partial \boldsymbol{\sigma}}^T = [-\frac{1}{2} + \frac{1}{2}sin(\phi^*_{friction}), \frac{1}{2} + \frac{1}{2}sin(\phi^*_f), 0, 0] \tag{37}$$

$$\frac{\partial g_1}{\partial \boldsymbol{\sigma}}^T = [-\frac{1}{2} + \frac{1}{2}sin(\psi^*), 0, 0, \frac{1}{2} + \frac{1}{2}sin(\psi^*)] \tag{38}$$

$$\frac{\partial g_2}{\partial \boldsymbol{\sigma}}^T = [-\frac{1}{2} + \frac{1}{2}sin(\psi^*), \frac{1}{2} + \frac{1}{2}sin(\psi^*), 0, 0] \tag{39}$$

The variation of the yield surfaces with respect to the hardening parameter '$\bar{\varepsilon}^{plastic}$' are:

$$\frac{\partial f_1}{\partial \bar{\varepsilon}^{plastic}} = \frac{\partial f_1}{\partial \phi^*_f}\frac{d\phi^*_f}{d\bar{\varepsilon}^{plastic}} + \frac{\partial f_1}{\partial c^*}\frac{dc^*}{d\bar{\varepsilon}^{plastic}} \tag{40}$$

Where:

$$\frac{\partial f_1}{\partial \phi^*_f} = \frac{1}{2}(\sigma_3 + \sigma_1)cos(\phi^*_f) + c^* sin(\phi^*_f) \tag{41}$$

$$\frac{\partial f_1}{\partial c^*} = -cos(\phi^*_f) \tag{42}$$

$$\frac{d\phi^*_{friction}}{d\bar{\varepsilon}^{plastic}} = \frac{\varepsilon^f * (\varepsilon^f - \bar{\varepsilon}^{plastic})sin(\phi_f)}{(\varepsilon^f \bar{\varepsilon}^{plastic})^{0.5}(\varepsilon^f + \bar{\varepsilon}^{plastic})^2\sqrt{1 - \frac{4\varepsilon^f \bar{\varepsilon}^{plastic} sin(\phi_f)^2}{(\varepsilon^f + \bar{\varepsilon}^{plastic})^2}}}; \text{for } \bar{\varepsilon}^{plastic} > 0 \tag{43}$$

$$\frac{dc^*}{d\bar{\varepsilon}^{plastic}} = -\frac{2c\bar{\varepsilon}^{plastic}\exp -\left(\frac{\bar{\varepsilon}^{plastic}}{\varepsilon^c}\right)^2}{\varepsilon^c} \tag{44}$$

Finally, the variation of the hardening parameter with respect to the plastic strains was devised as:

$$\frac{\partial \bar{\varepsilon}^{plastic}}{\partial \varepsilon^{plastic}} = (\sqrt{\frac{2}{3}}, \sqrt{\frac{2}{3}}, 0, \sqrt{\frac{2}{3}}) \tag{45}$$

References

[1] S. Krevor, H. de Coninck, S.E. Gasda, N.S. Ghaleigh, V. de Gooyert, H. Hajibeygi, R. Juanes, J. Neufeld, J. Roberts, F. Swennenhuis, Subsurface carbon dioxide and hydrogen storage for a sustainable energy future, Nat. Rev. Earth Environ. (2023) 1–17.

[2] C.R. Matos, J.F. Carneiro, P.P. Silva, Overview of large-scale underground energy storage technologies for integration of renewable energies and criteria for reservoir identification, J. Energy Storage 21 (2019) 241–258.

[3] G. Zhang, B. Li, D. Zheng, G. Ding, H. Wei, P. Qian, C. Li, Challenges to and proposals for underground gas storage (UGS) business in China, Nat. Gas Ind. B 4 (3) (2017) 231–237.

[4] D.J. Evans, R.A. Chadwick, Underground Gas Storage: Worldwide Experiences and Future Development in the UK and Europe, Geological Society of London, 2009.

[5] S. Sadeghi, B. Sedaee, Cushion and working gases mixing during underground gas storage: Role of fractures, J. Energy Storage 55 (2022) 105530.

[6] E. Bazdar, M. Sameti, F. Nasiri, F. Haghighat, Compressed air energy storage in integrated energy systems: A review, Renew. Sustain. Energy Rev. 167 (2022) 112701.

[7] L. Hashemi, M. Blunt, H. Hajibeygi, Pore-scale modelling and sensitivity analyses of hydrogen-brine multiphase flow in geological porous media, Sci. Rep. 11 (1) (2021) 1–13.

[8] M. Takach, M. Sarajlić, D. Peters, M. Kroener, F. Schuldt, K. von Maydell, Review of hydrogen production techniques from water using renewable energy sources and its storage in salt caverns, Energies 15 (4) (2022) 1415.

[9] M. Boon, H. Hajibeygi, Experimental characterization of H2/water multiphase flow in heterogeneous sandstone rock at the core scale relevant for underground hydrogen storage (UHS), Sci. Rep. 12 (2022) 14604.

[10] P. Fleuchaus, B. Godschalk, I. Stober, P. Blum, Worldwide application of aquifer thermal energy storage–A review, Renew. Sustain. Energy Rev. 94 (2018) 861–876.

[11] L. Feng, X. Zhang, X. Li, B. Li, Y. Li, Y. Xu, H. Guo, X. Zhou, H. Chen, Performance analysis of hybrid energy storage integrated with distributed renewable energy, Energy Rep. 8 (2022) 1829–1838.

[12] A. Olabi, M.A. Abdelkareem, Renewable energy and climate change, Renew. Sustain. Energy Rev. 158 (2022) 112111.

[13] R. Tarkowski, Underground hydrogen storage: Characteristics and prospects, Renew. Sustain. Energy Rev. 105 (2019) 86–94.

[14] S. Koohi-Fayegh, M.A. Rosen, A review of energy storage types, applications and recent developments, J. Energy Storage 27 (2020) 101047.

[15] J. Menéndez, A. Ordóñez, R. Álvarez, J. Loredo, Energy from closed mines: Underground energy storage and geothermal applications, Renew. Sustain. Energy Rev. 108 (2019) 498–512.

[16] S. Bauer, C. Beyer, F. Dethlefsen, P. Dietrich, R. Duttmann, M. Ebert, V. Feeser, U. Görke, R. Köber, O. Kolditz, et al., Impacts of the use of the geological subsurface for energy storage: An investigation concept, Environ. Earth Sci. 70 (8) (2013) 3935–3943.

[17] A. Amid, D. Mignard, M. Wilkinson, Seasonal storage of hydrogen in a depleted natural gas reservoir, Int. J. Hydrogen Energy 41 (12) (2016) 5549–5558.

[18] K. Ramesh Kumar, A. Makhmutov, C.J. Spiers, H. Hajibeygi, Geomechanical simulation of energy storage in salt formations, Sci. Rep. 11 (1) (2021) 1–24.

[19] A.A. Sainz-Garcia, Dynamics of Underground Gas Storage. Insights from Numerical Models for Carbon Dioxide and Hydrogen (Ph.D. thesis), Université Toulouse 3 Paul Sabatier (UT3 Paul Sabatier), 2017.

[20] T. Bai, P. Tahmasebi, Coupled hydro-mechanical analysis of seasonal underground hydrogen storage in a saline aquifer, J. Energy Storage 50 (2022) 104308.

[21] N. Heinemann, J. Alcalde, J.M. Miocic, S.J. Hangx, J. Kallmeyer, C. Ostertag-Henning, A. Hassanpouryouzband, E.M. Thaysen, G.J. Strobel, C. Schmidt-Hattenberger, et al., Enabling large-scale hydrogen storage in porous media–the scientific challenges, Energy Environ. Sci. 14 (2) (2021) 853–864.

[22] F. Crotogino, G.-S. Schneider, D.J. Evans, Renewable energy storage in geological formations, Proc. Inst. Mech. Eng., Part A: J. Power Energy 232 (1) (2018) 100–114.

[23] Z. Bo, M. Boon, H. Hajibeygi, S. Hurter, Impact of experimentally measured relative permeability hysteresis on reservoir-scale performance of underground hydrogen storage (UHS), Int. J. Hydrogen Energy (2023).

[24] K. Luboń, R. Tarkowski, Numerical simulation of hydrogen injection and withdrawal to and from a deep aquifer in NW Poland, Int. J. Hydrogen Energy 45 (3) (2020) 2068–2083.

[25] J. Chen, C. Du, D. Jiang, J. Fan, Y. He, The mechanical properties of rock salt under cyclic loading-unloading experiments, Geomech. Eng. 10 (3) (2016) 325–334.

[26] Y. Liu, T. Ma, H. Wu, P. Chen, Investigation on mechanical behaviors of shale cap rock for geological energy storage by linking macroscopic to mesoscopic failures, J. Energy Storage 29 (2020) 101326.

[27] X. Zhang, P. Tahmasebi, Effects of grain size on deformation in porous media, Transp. Porous Media 129 (1) (2019) 321–341.

[28] P. Jeanne, Y. Zhang, J. Rutqvist, Influence of hysteretic stress path behavior on seal integrity during gas storage operation in a depleted reservoir, J. Rock Mech. Geotech. Eng. 12 (4) (2020) 886–899.

[29] K. Kumar, H. Honorio, H. Hajibeygi, Simulation of the inelastic deformation of porous reservoirs under cyclic loading relevant for underground hydrogen storage, Sci. Rep. 12 (2022) 21404.

[30] B. Orlic, B. Wassing, C. Geel, Field scale geomechanical modeling for prediction of fault stability during underground gas storage operations in a depleted gas field in the Netherlands, in: 47th US Rock Mechanics/Geomechanics Symposium, OnePetro, 2013.

[31] F. Silverii, F. Maccaferri, G. Richter, B. Gonzalez Cansado, R. Wang, S. Hainzl, T. Dahm, Poroelastic model in a vertically sealed gas storage: A case study from cyclic injection/production in a carbonate aquifer, Geophys. J. Int. 227 (2) (2021) 1322–1338.

[32] P. Teatini, N. Castelletto, M. Ferronato, G. Gambolati, C. Janna, E. Cairo, D. Marzorati, D. Colombo, A. Ferretti, A. Bagliani, et al., Geomechanical response to seasonal gas storage in depleted reservoirs: A case study in the Po River basin, Italy, J. Geophys. Res.: Earth Surface 116 (F2) (2011).
[33] C. Janna, N. Castelletto, M. Ferronato, G. Gambolati, P. Teatini, A geomechanical transversely isotropic model of the Po River basin using PSInSAR derived horizontal displacement, Int. J. Rock Mech. Min. Sci. 51 (2012) 105–118.
[34] M. Cai, Practical estimates of tensile strength and Hoek–Brown strength parameter mi of brittle rocks, Rock Mech. Rock Eng. 43 (2) (2010) 167–184.
[35] P. Baud, V. Vajdova, T.-f. Wong, Shear-enhanced compaction and strain localization: Inelastic deformation and constitutive modeling of four porous sandstones, J. Geophys. Res.: Solid Earth 111 (B12) (2006).
[36] Y. Wang, C. Li, Y. Hu, X. Zhou, A new method to evaluate the brittleness for brittle rock using crack initiation stress level from uniaxial stress–strain curves, Environ. Earth Sci. 76 (23) (2017) 1–18.
[37] N. Brantut, M. Heap, P. Meredith, P. Baud, Time-dependent cracking and brittle creep in crustal rocks: A review, J. Struct. Geol. 52 (2013) 17–43.
[38] E. Hoek, Rock Fracture under Static Stress Conditions, CSIR, 1965.
[39] J.-c. Zhang, Z.-n. Lin, B. Dong, R.-x. Guo, Triaxial compression testing at constant and reducing confining pressure for the mechanical characterization of a specific type of sandstone, Rock Mech. Rock Eng. 54 (4) (2021) 1999–2012.
[40] T.-f. Wong, P. Baud, The brittle-ductile transition in porous rock: A review, J. Struct. Geol. 44 (2012) 25–53.
[41] C. Martin, N. Chandler, The progressive fracture of Lac du Bonnet granite, Int. J. Rock Mech. Min. Sci. Geomech. Abstracts 31 (1994) 643–659.
[42] R. Pijnenburg, B. Verberne, S. Hangx, C. Spiers, Inelastic deformation of the slochteren sandstone: Stress-strain relations and implications for induced seismicity in the groningen gas field, J. Geophys. Res.: Solid Earth 124 (5) (2019) 5254–5282.
[43] E. Hernandez, M. Naderloo, K.R. Kumar, H. Hajibeygi, A. Barnhoorn, Modeling of Cyclic Deformation of Sandstones Based on Experimental Observations, Vol. 2022, no. 1, European Association of Geoscientists & Engineers, 2022, pp. 1–5, URL https://www.earthdoc.org/content/papers/10.3997/2214-4609.202221120.
[44] E. Shalev, V. Lyakhovsky, A. Ougier-Simonin, Y. Hamiel, W. Zhu, Inelastic compaction, dilation and hysteresis of sandstones under hydrostatic conditions, Geophys. J. Int. 197 (2) (2014) 920–925.
[45] R. Pijnenburg, B. Verberne, S. Hangx, C. Spiers, Deformation behavior of sandstones from the seismogenic groningen gas field: Role of inelastic versus elastic mechanisms, J. Geophys. Res.: Solid Earth 123 (7) (2018) 5532–5558.
[46] A. Taheri, N. Yfantidis, C. Olivares, B. Connelly, T. Bastian, Experimental study on degradation of mechanical properties of sandstone under different cyclic loadings, Geotech. Test. J. 39 (4) (2016) 673–687.
[47] K. Peng, J. Zhou, Q. Zou, J. Zhang, F. Wu, Effects of stress lower limit during cyclic loading and unloading on deformation characteristics of sandstones, Constr. Build. Mater. 217 (2019) 202–215.
[48] R. Shen, T. Chen, T. Li, H. Li, W. Fan, Z. Hou, X. Zhang, Study on the effect of the lower limit of cyclic stress on the mechanical properties and acoustic emission of sandstone under cyclic loading and unloading, Theor. Appl. Fract. Mech. 108 (2020) 102661.
[49] K. Peng, J. Zhou, Q. Zou, X. Song, Effect of loading frequency on the deformation behaviours of sandstones subjected to cyclic loads and its underlying mechanism, Int. J. Fatigue 131 (2020) 105349.
[50] L.-j. Ma, X.-y. Liu, M.-y. Wang, H.-f. Xu, R.-p. Hua, P.-x. Fan, S.-r. Jiang, G.-a. Wang, Q.-k. Yi, Experimental investigation of the mechanical properties of rock salt under triaxial cyclic loading, Int. J. Rock Mech. Min. Sci. 62 (2013) 34–41.
[51] K. Fuenkajorn, D. Phueakphum, Effects of cyclic loading on mechanical properties of Maha Sarakham salt, Eng. Geol. 112 (1–4) (2010) 43–52.
[52] M.N. Bagde, V. Petroš, Fatigue properties of intact sandstone samples subjected to dynamic uniaxial cyclical loading, Int. J. Rock Mech. Min. Sci. 42 (2) (2005) 237–250.
[53] T. Zhenyu, M. Haihong, An experimental study and analysis of the behaviour of rock under cyclic loading, Intl. J. Rock Mech. Min. Sci. Geomech. Abs. 27 (1) (1990).
[54] Z. Li, F. Yang, J. Fan, D. Jiang, J. Ambre, Fatigue effects of discontinuous cyclic loading on the mechanical characteristics of sandstone, Bull. Eng. Geol. Environ. 81 (8) (2022) 1–15.
[55] B. Sun, Z. Zhu, C. Shi, Z. Luo, Dynamic mechanical behavior and fatigue damage evolution of sandstone under cyclic loading, Int. J. Rock Mech. Min. Sci. 94 (2017) 82–89.
[56] R. Geranmayeh Vaneghi, K. Thoeni, A.V. Dyskin, M. Sharifzadeh, M. Sarmadivaleh, Strength and damage response of sandstone and granodiorite under different loading conditions of multistage uniaxial cyclic compression, Int. J. Geomech. 20 (9) (2020) 04020159.
[57] D. Liang, N. Zhang, L. Xie, G. Zhao, D. Qian, Damage and fractal evolution trends of sandstones under constant-amplitude and tiered cyclic loading and unloading based on acoustic emission, Int. J. Distrib. Sens. Netw. 15 (7) (2019) 1550147719861020.
[58] Q. Meng, M. Zhang, L. Han, H. Pu, Y. Chen, Acoustic emission characteristics of red sandstone specimens under uniaxial cyclic loading and unloading compression, Rock Mech. Rock Eng. 51 (4) (2018) 969–988.
[59] Y. Wang, C. Deng, Z. Ding, F. He, X. Feng, D. Wang, Q. Hu, X. Zhao, Research on sandstone damage characteristics and acoustic emission precursor features under cyclic loading and unloading paths, Sustainability 14 (19) (2022) 12024.
[60] D. Yin, Q. Xu, Comparison of sandstone damage measurements based on non-destructive testing, Materials 13 (22) (2020) 5154.
[61] D. Jiang, K. Xie, J. Chen, S. Zhang, W.N. Tiedeu, Y. Xiao, X. Jiang, Experimental analysis of sandstone under uniaxial cyclic loading through acoustic emission statistics, Pure Appl. Geophys. 176 (1) (2019) 265–277.
[62] M. Naderloo, M. Moosavi, M. Ahmadi, Using acoustic emission technique to monitor damage progress around joints in brittle materials, Theor. Appl. Fract. Mech. 104 (2019) 102368.
[63] C.U. Grosse, M. Ohtsu, Acoustic Emission Testing, Springer Science & Business Media, 2008.
[64] K. Khaledi, E. Mahmoudi, M. Datcheva, T. Schanz, Stability and serviceability of underground energy storage caverns in rock salt subjected to mechanical cyclic loading, Int. J. Rock Mech. Min. Sci. 86 (2016) 115–131.
[65] A. Pouya, C. Zhu, C. Arson, Micro–macro approach of salt viscous fatigue under cyclic loading, Mech. Mater. 93 (2016) 13–31.
[66] B. Cerfontaine, R. Charlier, F. Collin, M. Taiebat, Validation of a new elastoplastic constitutive model dedicated to the cyclic behaviour of brittle rock materials, Rock Mech. Rock Eng. 50 (10) (2017) 2677–2694.
[67] X. Ding, G. Zhang, B. Zhao, Y. Wang, Unexpected viscoelastic deformation of tight sandstone: Insights and predictions from the fractional Maxwell model, Sci. Rep. 7 (1) (2017) 1–11.
[68] J. Wang, Q. Zhang, Z. Song, S. Feng, Y. Zhang, Nonlinear creep model of salt rock used for displacement prediction of salt cavern gas storage, J. Energy Storage 48 (2022) 103951.
[69] Q. He, F. Wu, R. Gao, Nonlinear creep-damage constitutive model of surrounding rock in salt cavern reservoir, J. Energy Storage 55 (2022) 105520.
[70] T. Xu, G. Zhou, M.J. Heap, S. Yang, H. Konietzky, P. Baud, The modeling of time-dependent deformation and fracturing of brittle rocks under varying confining and pore pressures, Rock Mech. Rock Eng. 51 (10) (2018) 3241–3263.
[71] S.Q. Yang, B. Hu, Creep and long-term permeability of a red sandstone subjected to cyclic loading after thermal treatments, Rock Mech. Rock Eng. 51 (10) (2018) 2981–3004.
[72] L.S. Tsai, Y.M. Hsieh, M.C. Weng, T.H. Huang, F.S. Jeng, Time-dependent deformation behaviors of weak sandstones, Int. J. Rock Mech. Min. Sci. 45 (2) (2008) 144–154.
[73] X. Li, Z. Yin, Study of creep mechanical properties and a rheological model of sandstone under disturbance loads, Processes 9 (2021).
[74] X. Wang, Q. Huang, B. Lian, N. Liu, J. Zhang, Modified Nishihara rheological model considering the effect of thermal-mechanical coupling and its experimental verification, Adv. Mater. Sci. Eng. 2018 (2018).
[75] P.A. Vermeer, R. De Borst, Non-associated plasticity for soils, concrete and rock, HERON 29 (3) (1984).
[76] J.P. Carter, C.P. Wroth, J.R.J.R. Booker, A critical state soil model for cyclic loading, in: Soil Mechanics - Transient and Cylic Loads, John Wiley & Sons Ltd, 1979, pp. 219–252.
[77] M.C. Weng, H.I. Ling, Modeling the behavior of sandstone based on generalized plasticity concept, Int. J. Numer. Anal. Methods Geomech. 37 (14) (2013) 2154–2169.
[78] R. de Borst, Integration of plasticity equations for singular yield functions, Comput. Struct. 26 (5) (1987) 823–829.
[79] Y.F. Dafalias, M. Asce, M.T. Manzari, A.M. Asce, Simple plasticity sand model accounting for fabric change effects, J. Eng. Mech. 130 (6) (2004) 622–634.
[80] M.C. Weng, A generalized plasticity-based model for sandstone considering time-dependent behavior and wetting deterioration, Rock Mech. Rock Eng. 47 (14) (2014) 1197–1209.
[81] J. Juez-Larre, G. Remmelts, J. Breunese, S. Van Gessel, O. Leeuwenburgh, Using underground gas storage to replace the swing capacity of the giant natural gas field of Groningen in the Netherlands. A reservoir performance feasibility study, J. Pet. Sci. Eng. 145 (2016) 34–53.
[82] K.H. Roscoe, J.B. Burland, On the generalized stress-strain behavior of wet clays, in: J. Heyman, F.A. Leckie (Eds.), Engineering Plasticity, 1968, URL https://www.researchgate.net/publication/264921746_On_the_Generalized_Stress-Strain_Behavior_of_Wet_Clays.
[83] O. Coussy, Poromechanics, Wiley, 2004, URL https://www.wiley.com/en-us/Poromechanics-p-9780470849200.
[84] M.A. Nikolinakou, G. Luo, M.R. Hudec, P.B. Flemings, Geomechanical modeling of stresses adjacent to salt bodies: Part 2 - Poroelastoplasticity and coupled overpressures, AAPG Bull. 96 (1) (2012) 65–85.
[85] D. Lockner, The role of acoustic emission in the study of rock fracture, Int. J. Rock Mech. Min. Sci. Geomech. Abstracts 30 (1993) 883–899.
[86] N. Gatelier, F. Pellet, B. Loret, Mechanical damage of an anisotropic porous rock in cyclic triaxial tests, Int. J. Rock Mech. Min. Sci. 39 (3) (2002) 335–354.
[87] B. Cerfontaine, R. Charlier, F. Collin, M. Taiebat, Validation of a new elastoplastic constitutive model dedicated to the cyclic behaviour of brittle rock materials, Rock Mech. Rock Eng. 50 (10) (2017) 2677–2694.
[88] P. Kelly, Solid Mechanics Lecture Notes - An Introduction to Solid Mechanics, University of Auckland, Auckland, New Zealand, 2013, p. 292.

[89] B. van der Pluijm, EARTH STRUCTURE: An Introduction to Structural Geology and Tectonics, second ed., W. W. Norton & Company, Inc, New York, NY, 2004.
[90] R. Weijermars, Principles of Rock Mechanics, sixth ed., Alboran Science Pub, hahran, Saudi Arabia, 1997.
[91] Fenix Consulting Delft B.V., 3D Geomechanical Model for Gas Storage Bergermeer Report for TAQA Energy BV, Technical Report, TAQA Energy BV, Delft, 2018, pp. 1–126.